

Measurement report: Microphysical and optical **characteristic characteristics** of radiation fog - a study using in-situ, remote sensing, and balloon techniques.

Katarzyna Nurowska^{1,2}, Przemysław Makuch³, and Krzysztof M. Markowicz¹

¹University of Warsaw, Faculty of Physics, Institute of Geophysics

²Guangdong Technion - Israel Institute of Technology, Department of Mathematics

³Polish Academy of Sciences, Institute of Oceanology

Correspondence: Katarzyna Nurowska (Katarzyna.Nurowska@fuw.edu.pl)

Abstract. ~~This~~ Based on in situ observations, remote sensing, and tethered balloon soundings, this study investigates the vertical profiles of microphysical and thermodynamic properties within radiative fog layers in the Strzyżów valley (Southeastern Poland), ~~based on in-situ, remote sensing and tethered balloon soundings data.~~ Across three case studies of radiation fog ~~that occurred~~ in September 2023, 74 soundings were performed, with 41 employing the OPC-N3 instrument to capture droplet spectra. The results indicated similar weather conditions in all cases, with a liquid water path consistently above $15 \text{ g}\cdot\text{m}^{-2}$, ~~although no transition to dense fog was observed~~ most observations remained within the thin fog regime. The effective droplet radius decreased with height (between $3\text{-}4.6 \mu\text{m}$ for 100 m), with larger droplets ($\geq 18.5 \mu\text{m}$) concentrated near the ground.

The fog dissipated both from Fog dissipation occurred simultaneously from both the top and bottom, ~~with the~~. The mature fog stage ~~marked by peak~~ was characterized by peaks in both liquid water content (LWC) and ~~the~~ droplet number concentration (N_c) near, typically located at approximately 80% of the fog height. ~~Theoretical calculations of droplet terminal velocity (total fog depth. Theoretical estimates of terminal velocity~~ for droplets $\geq 18.5 \mu\text{m}$) ~~indicate~~ suggest that larger droplets are removed from fog layers within minutes, affecting the longevity of the fog. ~~Equivalent~~ Calculated values of equivalent adiabaticity values (α_{eq} ~~the ratio~~, defined as the scaling factor by which the adiabatic lapse rate of the mixing ratio needs to be multiplied to ~~give the same amount of~~ match the observed liquid water path ~~as observed in a specific cloud~~) ~~ranged between~~ ranged from 0 ~~and to~~ 0.6. Except ~~in one instance where negative values for a single case where near-ground~~ α_{eq} ~~were observed near the ground, a phenomenon scarcely reported in existing fog studies~~ was negative — a phenomenon that is seldom documented in the fog literature.

Having instruments measuring radiation at two different heights (below and above the fog layer), it was possible to estimate the effect of fog on reducing ~~the~~ total shortwave and longwave (NET - downward - upward) radiation at ground level ~~by~~. Comparisons of NET radiation across the fog layer before and after its dissipation revealed differences of up to $150 \text{ W}\cdot\text{m}^{-2}$ (just before the fog disappearing and after). ~~The measured dependence of the reduction of longwave radiation by fog depends linearly on the amount of.~~ A linear relationship was observed between the reduction in longwave radiation and the liquid water path in our measurements; however, since all examined fog events were predominantly optically thin, this finding should be interpreted as applying primarily to optically thin fog conditions.

25 As a result of the measurements, average values of liquid water content and droplet number concentrations were obtained for the observed optically thin fogs in the valley area. Mean LWC in the fog layer core was found between 0.2–0.4 g·m⁻³, with N_c up to 300 cm⁻³. The ~~effective radius (near-surface mean effective radius ranged between 8 and 10 μm)and~~ exhibited a linear ~~height-dependent decrease, with radiation model closures yielding minimal biases, supporting decrease with height.~~ The good agreement between radiative transfer model outputs and observed radiative fluxes supports the accuracy of ~~radiation~~
30 ~~assessments within fog environments~~the retrieved microphysical parameters used as model inputs.

1 Introduction

A characteristic feature of radiation fogs is their localized nature, as they do not cover large areas, making their forecasting challenging. Weather conditions contribute to approximately 30% of aviation accidents in the USA ~~Gultepe (2023)~~(Gultepe, 2023). Radiation fog significantly reduces visibility and complicates navigation, posing a threat to transportation. According to the
35 American National Transportation Safety Board (NTSB), fog is the second most critical weather-related factor leading to fatal aviation accidents, accounting for an estimated 14% of such incidents ~~Capobianco and Lee (2001)~~(Capobianco and Lee, 2001). Fog ~~impacts-affects~~ not only safety but also ~~causes economic damage~~imposes significant economic costs. It can ~~lead to road~~
~~trafficedisruptions, sounding cancellations, and~~disrupt road traffic, force ships to alter their routes, and result in airport closures. ~~Based on the NTSB analysis~~In the United States, weather is the leading cause of aircraft delays, accounting for over 70% of
40 all cases (Kasper, 2016). Among weather-related factors, low visibility and low cloud ceilings are major contributors, as they require increased spacing between landing aircraft to maintain safety, thereby reducing airport throughput. According to NTSB data, visibility-related ~~effects contribute to aircraft-related delays approximately 30-35% of the time~~ Gultepe et al. (2019)
conditions contribute to approximately 30–35% of all flight cancellations (Stevens, 2019; Gultepe, 2023).

Fog is a meteorological phenomenon occurring near the Earth's surface, characterized by the suspension of water droplets in
45 the air, significantly reducing visibility to below 1 km ~~George (1951)~~(George, 1951). Several types of fog exist, depending on their formation mechanisms. This article focuses on radiation fog, which primarily forms at night under clear-sky and minimal wind conditions, within a stable boundary layer (SBL). Under such conditions, the ground surface cools significantly, leading to the cooling of the air immediately above it ~~Lakra and Avishek (2022)~~(Lakra and Avishek, 2022). Once the dew point temperature is reached, water vapor condenses on suspended particles (condensation nuclei), forming fog. This type of fog
50 develops from the ground upwards, usually not exceeding 200 meters in height. The cooling of successive air layers occurs from the lower layer upward, which is why radiation fogs are associated with the formation of temperature inversions. After sunrise, and with the onset of stronger winds, the fog and the inversion dissipate. When radiation fog forms, it initially remains optically thin to longwave (LW) radiation and develops within a stable lapse rate. When fog becomes optically thick, cooling occurs predominantly at the top of the fog layer, while the portion near the ground radiates in the LW range that is able to
55 warm the surface ~~Mason (1982); Price (2011)~~(Mason, 1982; Price, 2011). The potential equivalent temperature becomes uniform throughout the fog layer, inducing slight instability, which in turn increases turbulence within the fog. As demonstrated by Price (2011), approximately 50% of the fog cases he analyzed transitioned into optically thick, well-mixed fogs characterized

by a saturated adiabatic stability profile. His research suggests that this conversion typically occurs when the fog layer exceeds 100 meters in thickness. Numerical weather models have difficulty catching the shift from optically thin to optically thick ~~layer~~
60 ~~Poku et al. (2021); Boutle et al. (2022); Antoine et al. (2023)~~ fog (Poku et al., 2021; Boutle et al., 2022; Antoine et al., 2023).

~~The~~ Costablos et al. (2024) studied fog development during ~~the~~ SOFOG3D experiment. They proposed several methods ~~for~~
~~establishing if when occurs to identify the point at which~~ the transition from thin to optically thick fog ~~occurs~~:

- surface LW net radiation should approach ~~to~~ 0. In their research they assumed that this condition occurs when ~~$|\Delta LW| < 5$~~

65 ~~$|LW_N| < 5 \text{ W}\cdot\text{m}^{-2}$~~

- ~~profile of air temperature (T) decreases~~ ~~the air temperature profile within the fog layer should decrease~~ with height, ~~due~~
~~to warming the surface and cooling at the top of fog~~. They were checking this condition if T at 50 m is lower than T
~~at as the air near the surface is warmed by the ground while the fog top cools radiatively. They checked whether the~~
~~temperature gradient was negative by comparing temperatures at 25 m and 50 m.~~

70 – turbulent kinetic energy exceeds $0.10 \text{ m}^2\cdot\text{s}^{-2}$,

- fog top height exceeds 110 m,

- Wærsted et al. (2017) proposed ~~LWP <~~ ~~that a transition to optically thick fog occurs when LWP >~~ $30 \text{ g}\cdot\text{m}^{-2}$, ~~however~~
~~Costablos et al. (2024) found that in SOFOG3D experiment this value is too high. They proposed that LWP >~~ ~~but~~
75 ~~Costablos et al. (2024) suggested a value of $15 \text{ g}\cdot\text{m}^{-2}$~~ , ~~so it more matches to match more closely~~ the time when ~~the~~
other criteria are met.

Those conditions were met in ~~the~~ SOFOG3D experiment ~~closely in time within around~~ ~~within about~~ 1 hour.

Key factors influencing the likelihood of fog transitioning into an optically thick state include the time of its forma-
tion (the ~~more time earlier~~ before sunrise, the ~~better more likely~~) and the humidity profile of the air ~~Boutle et al. (2018)~~
~~(Boutle et al., 2018)~~. For droplets to begin forming, aerosols acting as cloud condensation nuclei (CCN), such as ~~for example~~
80 ammonium nitrate aerosols, are required. In clouds, turbulence can uplift air masses, activating CCNs more rapidly and ex-
tensively. In fog, droplet growth is primarily governed by radiative cooling. As demonstrated by Boutle et al. (2018), a higher
concentration of large aerosol particles accelerates the transition to a well-mixed fog state. Additionally, the type of aerosol
present in the air is important; compounds with high hygroscopicity that can activate at low supersaturation levels are most
effective as CCN ~~Gilardoni et al. (2014)~~ ~~(Gilardoni et al., 2014)~~.

85 According to Costablos et al. (2024), during ~~the~~ SOFOG3D, inverted LWC profiles—maximum LWC found at the ground
and decreasing with altitude—were commonplace in optically thin fogs. Mostly in well-mixed optically thick fogs, quasi-
adiabatic profiles with LWC increasing with height were found. However, in one case, they measured LWC profiles decreasing
with height one hour after the transition occurred and LWC values at the ground reached $0.25 \text{ g}\cdot\text{m}^{-3}$, the highest values recorded
during ~~the~~ whole campaign.

90 Research utilizing cloud radars, ceilometers, and microwave radiometers has ~~established~~made it possible to establish the rate at which LW radiative cooling ~~can produce water within fog. For fogs with a~~at the top of the fog layer can lead to condensation within the fog. Under clear-sky conditions, when the liquid water path (LWP) ~~exceeding exceeds~~ $30 \text{ g}\cdot\text{m}^{-2}$ ~~under clear-sky, this rate is approximately~~, this cooling (above the fog) can result in the formation of liquid water at a rate of up to $70 \text{ g}\cdot\text{m}^{-2}\cdot\text{h}^{-1}$ ~~Wærsted et al. (2017).~~(Wærsted et al., 2017).

95 The presence of clouds above the fog can also influence water condensation, with low clouds potentially blocking cooling entirely, leading to fog dissipation.

After sunrise, shortwave (SW) radiation begins to heat the fog, causing droplet evaporation. Wærsted et al. (2017) estimated that the strength of this process is about $10\text{-}15 \text{ g}\cdot\text{m}^{-2}\cdot\text{h}^{-1}$. The rate of evaporation increases with the effective radius of droplets (r_{eff}) and LWP, and decreases with larger solar zenith angles. Additionally, the warming of the ground surface transfers
100 approximately $30 \text{ g}\cdot\text{m}^{-2}\cdot\text{h}^{-1}$ of sensible heat to the fog.

To accurately predict the formation and evolution of fog, a weather forecasting model must effectively represent the interactions between the atmosphere and the Earth's surface, various processes (such as microphysics, radiation, and turbulence), and it must do so on a local scale while accounting for terrain features.

One approach to studying fog is through large-eddy simulations (LES) modeling. This approach enables the examination of
105 turbulence effects and interactions between the atmosphere and the surface ~~Maronga and Bosveld (2017)~~(Maronga and Bosveld, 2017), the deposition of droplets on vegetation ~~Mazoyer et al. (2017)~~(Mazoyer et al., 2017), or the influence of the urban canopy ~~Bergot et al. (2015)~~(Bergot et al., 2015) on fog formation and evolution. Numerical models often struggle to accurately forecast fog formation, dissipation, depth, or water content ~~Román-Cascón et al. (2012); Zhou et al. (2012); Bari et al. (2023)~~(Román-Cascón et al., 2012); Zhou et al. (2012); Bari et al. (2023). This difficulty arises from the fog's localized nature and the delicate balance between processes such as radiation balance,
110 droplet deposition on the surface, turbulent mixing, microphysical properties, and moisture availability. Recently, AI-based tools, including machine learning and deep learning, have been employed to enhance numerical weather prediction (NWP). While these methods have shown promising results, they also introduce new challenges. Machine learning requires high-quality datasets specific to each forecast location, as well as substantial computational resources to produce timely results ~~Bari et al. (2023)~~(Bari et al., 2023).

115 For the initialization of numerical models or the development of methods to retrieve LWP from satellites, it is essential to understand the microphysical properties of fog as a function of height. Unfortunately, there is a scarcity of data on the vertical distribution of fog's microphysical characteristics. Measurements using aircraft are impractical because fog typically forms close to the Earth's surface and inherently reduces visibility. However, measurements can be conducted using aerological balloons Egli et al. (2015), instrumentation placed on tall towers Ye et al. (2015); Han et al. (2018), and more recently, drones
120 and microwave radiometers (MWR) have become viable options for such observations.

Using a tethered balloon, Pinnick et al. (1978) made the first measurements of the vertical profiles of microphysical characteristics in fog. ~~He~~They showed that in the studied cases, a fog had a bimodal distribution of droplets ($r=5 \mu\text{m}$ and $r=0.6 \mu\text{m}$) with LWC range from 10^{-4} to $0.45 \text{ g}\cdot\text{m}^{-3}$.

Egli et al. (2015) performed soundings with a tethered balloon, and measured LWC, N_c and r_{eff} every 10 m. His results from two fog cases show that the changes in LWC are related to the change in N_c and not to the change in droplet size. In most cases, r_{eff} was constant with height. One fog case was characterised by low LWC (maximum of $0.14 \text{ g}\cdot\text{m}^{-3}$) however, however, high N_c above 2000 cm^{-3} . In this case of fog, 3 measurements were taken. Omitting the values of r_{eff} at the very bottom of the profiles (where the values dropped significantly), the value of r_{eff} decreased with height. In the case of one profile, the value of r_{eff} at a 25 m reached a maximum of $9.4 \mu\text{m}$. ~~Second-The second~~ fog case, ~~within-with~~ six soundings, ~~eonsist-consisted~~ of a considerably thicker fog with higher LWC and r_{eff} values, although accompanied by lower total drop counts. The LWC had a constant pattern in the first third of the height, then LWC increased with height, and then decreased with height to the cloud top. The highest LWC value was $0.54 \text{ g}\cdot\text{m}^{-3}$. N_c had a similar pattern with height as LWC. The highest N_c value recorded was 500 cm^{-3} . The r_{eff} values differ from sounding to sounding, however they were constant with height, in range between 4 and $8 \mu\text{m}$.

The motivation for this study is the miniaturization of equipment for particle detection. For example, the Alphasense OPC-N3 - optical particle matter (PM) sensor, commonly used for aerosol monitoring, can also be used to measure the microphysical properties of fog when mounted on a tethered balloon or drone (Nurowska et al. (2023))(Nurowska et al., 2023). Such a system was employed to capture vertical profiles of radiative fog in a mountain valley, a region where air pollution can be elevated during inversion conditions. This type of terrain enables fog monitoring at different altitudes. In this setup, SW and LW radiometers positioned near the valley bottom and mountain top allow for determining determination of the optical, microphysical, and radiation closure of the fog. Section 2 outlines the instruments utilized for conducting the measurements, while Section 3 details the methodology of the in-situ measurements and the model setup. The core of the article is presented in Section 4, which features a case study of radiative fog occurrence, including optical, microphysical, and radiation closure analyses performed for this case. Section 4 focuses on an event in the Strzyżów valley, where data were gathered using a balloon. The 1D Fu-Liou radiative transfer model (Fu and Liou, 1992, 1993) was applied to simulate the conditions in the Strzyżów valley, incorporating additional data from the SolarAOT station (which consists of an upper and lower station).

2 Experiment setup

This study is based on measurements taken at two sites in the Strzyżów. This a small town is located in Southern Poland in region of southern Poland, in the region of the Strzyżowskie Foothills foothills. The city is located next to the river Wisłok River. The research was conducted using remote sensing and in-situ in situ techniques as well as by an apparatus connected to a tethered balloon. In addition, numerical stimulation simulations were used for the radiation closure study.

2.1 SolarAOT^{upper} station_{lower} - launching site

The balloon launching site was located on a slope of a hill. The lower station is located in the valley of Strzyżów city at 260 m.a.s.l. of valley of Strzyżów city. Next to the town is situated a SolarAOT – a private radiative transfer research station which collaborates with University of Warsaw. The location of both stations is shown on Fig. 1. Location of tethered balloon

160 ~~launching site SolarAOT_{lower} and SolarAOT^{upper} station, in relation to the Strzyżów city and the Wisłok river. (49°52'18.0"N~~
~~21°48'26.0"E). On the site of balloon launching, there was mounted a CNR4 net radiometer for upward and downward SW~~
~~and LW flux; a meteo station including MetPak and sensors A100LK, W200P, HYT936, and OPC-N3. In addition, the mobile~~
~~laboratory equipped with Aurora 4000 nephelometer, Laser Aerosol Spectrometer LAS 3340A, and Oxford Lasers VisiSize~~
~~D30 (ShadowGraph) was used at this site. Raymetrics single-wavelength (532 nm) lidar 510M for aerosol and cloud detection~~
~~was used.~~

165 ~~The VisiSize D30 system, developed by Oxford Lasers Ltd., operates using the shadowgraph technique. The VisiSize~~
~~D30, hereafter referred to as ShadowGraph, captures shadow images of particles as they pass through the measurement~~
~~volume between a laser head and a high-resolution camera. This system enables the determination of microphysical properties,~~
~~including particle shape, size, droplet size distribution (DSD(r)), total droplet number concentration, and liquid water content~~
~~(LWC).~~

170 ~~The ShadowGraph system has been effectively utilized in the study of cloud microphysics, both in laboratory settings~~
~~and during in situ measurements. The droplet detection and sizing mechanisms of the ShadowGraph were comprehensively~~
~~detailed by (Nowak et al., 2021). Data collected using the ShadowGraph in studies of orographic clouds, specifically under~~
~~foggy conditions in mountainous regions, were analyzed by (Mohammadi et al., 2022).~~

~~During this campaign, the ShadowGraph was used for two purposes: first, as the reference instrument to which the OPC-N3~~
~~was calibrated, as demonstrated in Nurowska et al. (2023); and second, to monitor conditions near the surface. The ShadowGraph~~
~~operates using a high-power laser with a wavelength invisible to the human eye. For safety reasons, it was installed on the roof~~
~~of the mobile laboratory, approximately 3 m above ground level.~~

175 **2.2 SolarAOT^{upper} station**

~~SolarAOT^{upper} - is a private radiative transfer research station (~~collaborates with which collaborates with the~~ University of~~
~~Warsaw) ~~is~~ located in an agricultural area on one of the peaks of the Niebylecka Mountain ~~on at~~ 445 m a.s.l. (49°52'43.0"N~~
~~21°51'40.8"E), located from Strzyżów city in a straight line 4 km, vertical height difference 185 m. ~~At the~~ ~~The location~~~~
~~of both stations is shown on Fig. 1. At the SolarAOT^{upper} station are mounted several instruments, inter alia, pyranome-~~
~~ter CMP21, Eppley pyrgeometer, CIMEL, Nephelometer Aurora 4000, Aethalometr AE-31, ~~CHM-15K ceilometr, lidar,~~ and~~
~~RPG-HATPRO-G5. ~~CHM-15K ceilometer.~~~~

185 ~~A Kipp & Zonen CMP21 pyranometer was used to measure downwelling shortwave radiation (285–2800 nm), including~~
~~both direct solar and diffuse sky components. For longwave radiation, an Eppley pyrgeometer was employed, operating in the~~
~~spectral range of approximately 4.5 to 50 μ m, to capture downwelling infrared radiation emitted by the atmosphere and clouds.~~
~~Both sensors were installed on a leveled platform in an unobstructed area.~~

~~CIMEL is an instrument for measuring direct and scattered solar radiation in 9 spectral channels: 340, 380, 440, 500, 675,~~
~~870, 936, 1020, 1640 nm. Based on the measured values, the optical parameters of the aerosol are determined, including the~~
~~AOD ~~or the Angstrom and the Ångström~~ exponent. The data collected by the instrument is processed within the international~~

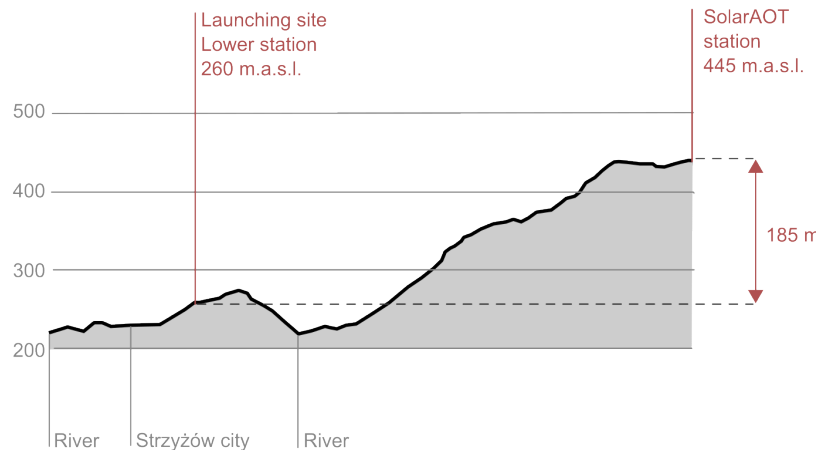


Figure 1. Location of tethered balloon launching site SolarAOT_{lower} and SolarAOT^{upper} station, in relation to the Strzyżów city and the Wisłok river.

AERONET measurement network. Nephelometer Aurora 4000 is used to measure light scattering coefficients on aerosols for
 190 wavelengths of 450, 525, 630 nm in 18 ranges of aerosol scattering angles. ~~Aethalometr-~~

~~Aethalometer~~ AE-31 is used to measure the concentration of equivalent ~~of~~ black carbon (eBC) in the atmosphere and the aerosol absorption coefficient of the aerosol. The measurement is performed at 7 wavelengths (370, 470, 520, 590, 660, 880, 950 nm) using the method of changing the transmission of a quartz filter on which the aerosol is deposited.

2.3 ~~SolarAOT_{lower} - launching site~~

195 ~~The lower station is located at valley of Strzyżów city at 260 m.a.s.l. (49°52'18.0"N 21°48'26.0"E). On the site of balloon launching there was mounted CNR4 net radiometer for upward and downward SW and LW flux; meteo station including MetPak and sensors A100LK, W200P, HYT936, OPC-N3. In addition, the mobile laboratory equipped with Aurora 4000 nephelometer, Laser Aerosol Spectrometer LAS 3340A, and Oxford Lasers VisiSize D30 (ShadowGraph) was used at this site. Raymetrics single wavelength (532 nm) lidar 510M for aerosol and cloud detection was used-~~

200 ~~The VisiSize D30 system, developed by Oxford Lasers Ltd., operates using the shadowgraph technique. The VisiSize D30, hereafter referred to as ShadowGraph, captures shadow images of particles as they pass through the measurement volume between a laser head and a high-resolution camera. This system enables the determination of microphysical properties, including particle shape, size, droplet size distribution (DSD(r)), total droplet number concentration, and liquid water content (LWC)-~~

205 ~~The ShadowGraph system has been effectively utilized in the study of cloud microphysics, both in laboratory settings and during in situ measurements. The droplet detection and sizing mechanisms of the ShadowGraph were comprehensively detailed by Nowak et al. (2021). Data collected using the ShadowGraph in studies of orographic clouds, specifically under~~

~~foggy conditions in mountainous regions, were analyzed by Mohammadi et al. (2022). In our measurements we treat this instrument as reference instrument to which are calibrated OPC-N3, as have been showed in article Nurowska et al. (2023).~~

210 2.3 Balloon apparatus

~~For measurements were used~~ Measurements were conducted using two meteorological balloons (for better buoyancy), each approximately 1.5 meters in diameter and filled with helium. ~~Balloon was~~ The balloons were tethered using the Vaisala TTW111 Winch winch (see Figure 2a). Around two ~~meters below balloon~~ metres below the balloon, the apparatus was mounted on the rope holding the balloon. The ~~set up used at apparatus used to mount below~~ the balloon was (see Figure 2b):

- 215 – Vaisala radiosonde RS41 - collecting data about pressure (p), ~~T~~ temperature (T), relative humidity (RH),
- GY-63 MS5611 - a ~~high performance~~ high-performance pressure sensor module,
- HYT 939 - additional T and ~~realtive humidity~~ RH sensor,
- The Alphasense OPC-N3 - ~~optical partiele matter (PM) an optical particle~~ sensor that measures ~~mass concentration in size range~~¹ particle counts across size bins ranging from 0.35 to 40 μm , as well as $\text{PM}_{1.0}$ ¹, $\text{PM}_{2.5}$ and PM_{10} ~~mass concentration, however here.~~ Here, OPC-N3 was used to gather ~~the data information~~ about fog droplets based on ~~article Nurowska et al. (2023)~~ the article (Nurowska et al., 2023), such as liquid water content (LWC), effective radius r_{eff} and N_c .
- SENSIRION SPS30 - optical PM sensor that measures $\text{PM}_{1.0}$, $\text{PM}_{2.5}$, PM_4 , PM_{10} mass concentration
- TFMini - visibility sensor
- 225 – AE-51 - miniature aethalometer for measuring the eBC concentration and the aerosol absorption coefficient at a wavelength of 880 nm.

~~not all the time the radiosonde, AE-51 was present – due to the weight of the balloon and its buoyancy.~~

The OPC-N3, an optical particle counter designed by Alphasense Ltd., utilizes a diode laser emitting light at a wavelength of 658 nm, along with an elliptical mirror that directs the laser beam towards a detector. The airflow, driven perpendicularly
230 to the laser beam by an integrated fan, allows for continuous operation. The OPC-N3 quantifies particle number concentration (~~N_c~~ N_c) across 24 size bins, covering a diameter range from 0.35 to 40 ~~μm~~ μm . The onboard algorithm converts ~~N_c~~ N_c measurements into PM_{10} , $\text{PM}_{2.5}$, and PM_{10} values. Detailed ~~specifications~~ specification of the OPC-N3 is available in the work by ~~Hagan and Kroll (2020)~~ (Hagan and Kroll, 2020).

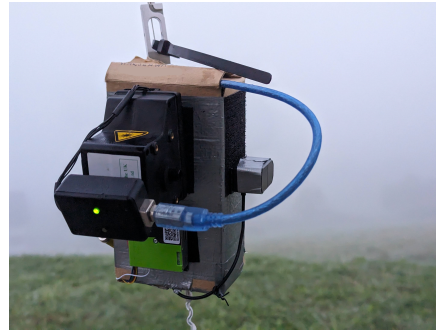
OPC-N3 devices are considered low-cost sensors, which means that two identical units may not yield consistent results due to
235 device-to-device variability. Therefore, cross-calibration between sensors or calibration against a reference-grade instrument is

¹ ~~number after PM denotes size range up to this size in μm~~

¹ The number after PM denotes particles with diameters up to the given size in μm which are counted.



(a) Balloon with attached payload and connected to the winch.



(b) Zoom to the balloon payload, showing: inside the box (GY-63, HYT 939), OPC-N3, SPS30, TFMini

Figure 2. Balloon setup.

necessary to ensure measurement accuracy. Additionally, individual OPC-N3 units may exhibit signal drift over time, requiring periodic recalibration to maintain data reliability.

240 For this reason, it was not possible to directly use the calibration parameters provided in (Nurowska et al., 2023). Instead, the calibration had to be repeated following the methodology described in that work, to ensure compatibility with the specific sensors used in this study. OPC-N3 was calibrated to the ShadowGraph following (Nurowska et al., 2023). Results of N_c , LWC and r_{eff} were obtained by taking bins of OPC-N3 measuring particles greater than $1.15 \mu\text{m}$ (bin 7 of OPC-N3).

The calibration equations used between OPC-N3 and Shadowgraph are:

$$\underline{LWC_{\text{ShadowGraph}} = 6.15 \cdot LWC_{\text{OPC-N3}} + 0.11} \quad (1)$$

$$245 \quad \underline{N_{c\text{ShadowGraph}} = 4.16 \cdot N_{c\text{OPC-N3}} + 32.63} \quad (2)$$

$$\underline{r_{\text{eff}}^{\text{ShadowGraph}} = 0.70 \cdot r_{\text{eff}}^{\text{OPC-N3}} + 3.81} \quad (3)$$

The OPC-N3 allows calculation of the volume droplet size distribution (vDSD), which can be computed using the formula:

$$\underline{vDSD(r_b) = N_b \cdot (\Delta r_b \cdot V_b)^{-1} \cdot r_b^3} \quad (4)$$

250 where N_b is the number of droplets in a bin, V_b the volume of a bin, Δr_b is the width of the bin and r_b is the mean bin droplet radius. Although the obtained vDSD was not calibrated against the ShadowGraph, it provides information on which droplet sizes contribute most significantly to the LWC at a given altitude.

3 Methodology and model set up

3.1 Balloon measurements methodology

255 For three days between 9 - 11 September 2023, the measurements of radiative fog were held made in Strzyżów city, Poland. The balloon launch site was located in the valley of Strzyżów city. ~~Two meteorological balloons (for better buoyancy) filled with helium (to around 1,5 m diameter) were tethered using the Vaisala TFW111 Winch. Below the balloons was attached apparatus to the winch rope.~~ Four setups were used, as it was not possible due to the buoyancy to mount all instruments at once:

- 260
- setup 1: GY-63, HYT 939, OPC-N3, SPS30, TTFMini - this setup was most common
 - setup 2: only Vaisala radiosonde RS41
 - setup 3: Vaisala radiosonde RS41, AE-51.
 - setup 4: Vaisala radiosonde RS41, GY-63, HYT 939, OPC-N3, SPS30, TTFMini.

Figure 3 shows with colored lines when, during the night, the soundings were done, with colors are indicated indicating different setups mounted on the balloon. The same information, but with specific sounding times, can be found in the Appendix A1. In total there were 74 soundings, however due to problems with data recording were conducted. However, due to data recording issues, 11 soundings are missing all or some lacked complete data and were not taken into account in further analysis (marked in Figure excluded from further analysis. These are indicated in gray in Figure 3 and Table A1 in gray). Sounding A1. Soundings were done by unwinding the rope until it started to tilt to the horizon. The balloon was stopped for a few seconds, and the line was wound up. Soundings were done with around 15 minutes brakes 15-minute breaks in between.

270

The fog case description was divided into 3 phases stages: initial, developed, and decaying. The transition from initial phase to developed the initial to the developed stage was assumed to occur when $LWP > 15 \text{ g} \cdot \text{m}^{-2}$, the change from mature to decaying was assumed when $LWP < 15 \text{ g} \cdot \text{m}^{-2}$.

Table 1 presents information about each fog stage.

275 During campaign ShadowGraph was used for two purposes, one to calibrate OPC-N3 and other to monitor situation near surface. As ShadowGraph works on the basis of a considerable power laser with invisible to the human eye light, for safety purposes, it was placed on the roof of the mobile laboratory at a height of approx. 3 m above the ground. OPC-N3 was used measure the N_c ; the r_{eff} and the LWC. OPC-N3 was calibrated to the ShadowGraph following Nurowska et al. (2023). Results of $N_{c, \text{droplets}}$, LWC and r_{eff} were obtained by taking bins of OPC-N3 measuring particles greater than $1.15 \mu\text{m}$ (bin 7 of OPC-N3).

280

The calibration equations between used OPC-N3 and Shadowgraph are:

$$\underline{LWC_{\text{ShadowGraph}} = 6.15 \cdot LWC_{\text{OPC-N3}} + 0.11}$$

$$\underline{N_{c, \text{ShadowGraph}} = 4.16 \cdot N_{c, \text{OPC-N3}} + 32.63}$$

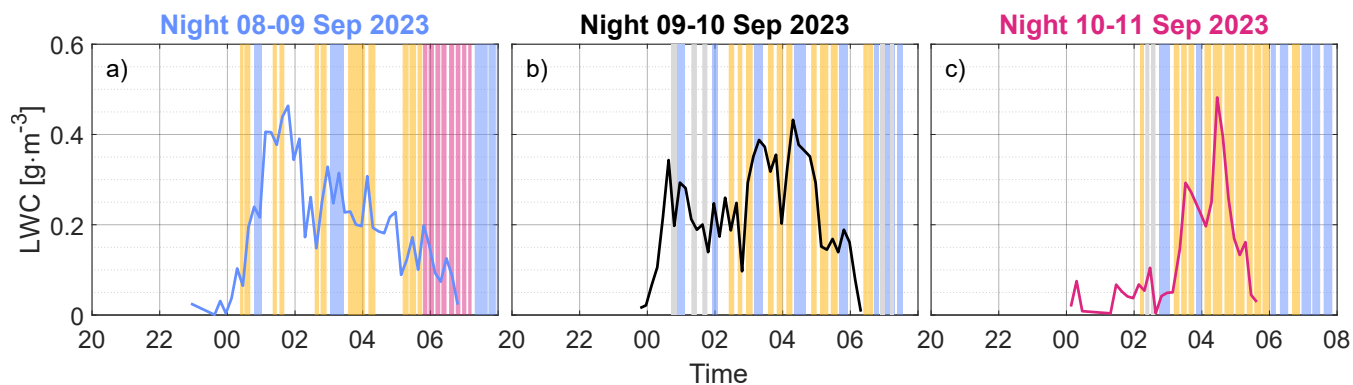


Figure 3. Figure visualize when The figure illustrates the timing of the soundings where done,; different colors presents what apparatus was represent the specific equipment configurations mounted on the balloon: orange - setup with OPC-N3, blue - setup with radiosonde, pink - setup with OPC-N3 and radiosonde, gray - problems with collected data. The image is overlaid on the line representing temporal variability of the LWC at the ground obtained from Shadowgraph (the same figure data as on Fig. 5).

Fog episode		Stage		
		Initial	Developed	Decaying (soundings after fog vanishing)
Night 8-9	Time	23:00 - 2:34	2:34 - 6:42	6:45 - 7:00 (8:10)
	Profiles with OPC-N3	4	12	2(+1)
	Profiles with Radiosonde	1	6	2 (+4)
Night 9-10	Time	00:00 - 2:45	2:45 - 6:00	6:00 - 7:30
	Profiles with OPC-N3	0	9	2
	Profiles with Radiosonde	1	4	3
Night 10-11	Time	2:00 - 3:02	3:02 - 5:30	5:30 - 6:00 (8:00)
	Profiles with OPC-N3	1	7	2 (+1)
	Profiles with Radiosonde	1	2	0 (+5)

Table 1. Times of initial, developed and decaying stage of observed fogs on days 9 - 11 Sep., with information on how many soundings were performed in each period.

$$r_{\text{eff}}^{\text{ShadowGraph}} = 0.70 \cdot r_{\text{eff}}^{\text{OPC-N3}} + 3.81$$

One sounding consisted of launching the balloon, at some point the balloon was no more going upward (but started to move horizontally) then the winch was stopped and started to wind up the winch string. During one balloon launch, we obtained two vertical profiles, which were then averaged over height to obtain an image less noisy by a less noisy image due to random fluctuations. All the data were interpolated every 1 m for making figures. On the plots soundings starts, soundings start at 2 m above ground.

The OPC-N3 allows to calculate volume droplet size distribution (vDSD) which can be computed using formula:-

$$\text{vDSD}(r_b) = N_b \cdot (\Delta r_b \cdot V_b)^{-1} \cdot r_b^3$$

where N_b is the number of droplets in a bin, V_b the volume of a bin, Δr_b the width of the bin and r_b the mean bin droplet radius. The obtained vDSD was not calibrated with ShadowGraph. vDSD gives information which droplets give biggest contribution to LWC at specific height-

3.2 Adiabatic LWC

Equivalent adiabaticity (α_{eq}) relates theoretical adiabatic LWC profiles to observed ones. It has been used in studies aiming to estimate cloud base height or improve fog forecasting based on satellite data. For instance, Cermak and Bendix (2011) proposed a model comparing theoretical and satellite-derived LWP to infer cloud base height, while Toledo et al. (2021) applied a similar approach to model fog dissipation. In this section, we present the theoretical derivation of α_{eq} , which is defined as the scaling factor applied to the adiabatic LWC profile to match the theoretical LWP with the observed value.

To describe the change of LWC in a perfect adiabatic cloud, the following equation is used (5) (Cermak and Bendix (2011); Toledo et al. (2021); Cermak and Bendix, 2011; Toledo et al., 2021; Costablos et al., 2024).

$$\frac{d\text{LWC}(z)}{dz} = \Gamma_{ad}(T(z), p(z)) \quad (5)$$

where z - is height calculated from the base of the cloud. $\Gamma_{ad}(T(z), p(z))$ is the negative of the change in saturation mixing ratio with height for an ideal adiabatic cloud; in other words it is, it is the adiabatic condensation rate. The processes in stratus clouds are nearly adiabatic; the deviation from adiabatic conditions is introduced into the equation as a parameter α . The fog is similar to stratus cloud, however; however, to integrate Equation 5 apart from adding α , a non-zero surface liquid water content (LWC_0) must be taken into account.

$$\text{LWC}(z) = \int_{z'=0}^{z'=z} \alpha(z') \Gamma_{ad}(T(z'), p(z')) dz' + \text{LWC}_0 \approx \Gamma_{ad}(T_B, p_B) \int_{z'=0}^{z'=z} \alpha(z') dz' + \text{LWC}_0 \quad (6)$$

LWP is defined as:

$$\text{LWP} = \int_{z'=0}^{z'=CTH} \text{LWC}(z') dz' \quad (7)$$

as fog base is at ground ~~the integration take~~, the integration takes place from z' equal zero to cloud/fog top height (CTH).

315 In the case of shallow clouds $\Gamma_{ad}(T(z), p(z))$ can be assumed constant with height Brenguier (1991) $\Gamma_{ad}(T_B, p_B) = const.$ where T_B and p_B are respectively temperature and pressure at fog base/ground. Since the dependence of $\alpha(z)$ is unknown, the concept of equivalent adiabaticity $\alpha_{eq} = const.$ is introduced. The α_{eq} is defined as the constant adiabaticity value that would give the same LWP value when replacing $\alpha(z')$ in Eq. 6 and calculating LWP from Eq. (7). After taking $\alpha_{eq} = const.$ the formula for LWP becomes:

$$320 \quad LWP = \frac{1}{2} \alpha_{eq} \Gamma_{ad}(T_B, p_B) \cdot CTH^2 + LWC_0 \cdot CTH \quad (8)$$

The formula for LWC with the above assumptions is:

$$LWC(z) = \alpha_{eq} \Gamma_{ad}(T_B, p_B) \cdot z + LWC_0 \quad (9)$$

The method of calculating $\Gamma_{ad}(T_B, p_B)$ was taken ~~the same as in~~ from Appendix A of the article ~~Toledo et al. (2021)~~ (Toledo et al., 2021)

325 To calculate what α_{eq} is, just reverse the Equation 8

$$\alpha_{eq} = \frac{2(LWP - LWC_0 \cdot CTH)}{\Gamma_{ad}(T_B, p_B) \cdot CTH^2} \quad (10)$$

In the literature, instead of α_{eq} , the parameter β is sometimes used, introduced by Betts (1982) as the in-cloud mixing parameter. This parameter measures departure from the adiabatic situation. The relation between α_{eq} and β is $\alpha_{eq} = 1 - \beta$.

~~In order to determine the existence of ground fog from satellite data, Cermak and Bendix (2011) proposed the LWC model for fog and stratus clouds. It is based on comparing the LWP obtained from the theoretical LWC profile with the height Eq. (8), with satellite data on LWP, CTH and T(CTH). In this way, it is possible to calculate the height of the cloud base. Toledo et al. (2021) based on Eq. (8) developed a one-column conceptual model of adiabatic continental fog to improve nowcasting of fog dissipation.~~

In ~~later~~ the latter part of this article will be used:

- 335
- Γ_{ad} - adiabatic condensation rate of LWC,
 - α_{eq} - ~~deviation from~~ scaling of Γ_{ad} , which would give the same LWP for the whole cloud/fog,
 - α_{fit} - ~~deviation from~~ scaling of Γ_{ad} obtained by fitting line to LWC dependence from height.
 - Γ_{wa} - moist adiabatic lapse rate for T,
 - γ_{fit} - ~~deviation from~~ scaling of Γ_{wa} obtained by fitting line to T dependence from height.

340 The Fig. 4 presents the visualization of ~~listed above concepts~~ the concepts listed above.

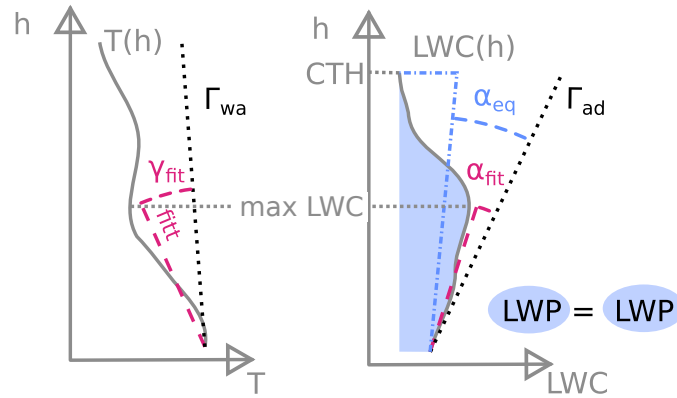


Figure 4. Representation of profile of T and LWC with added lines of Γ_{wa} and Γ_{ad} respectively. The γ_{fit} and α_{fit} represents the angle between best line fit to T and LWC respectively (from bottom to height of max LWC) and Γ_{wa} and Γ_{ad} represents the angle between the best line fit to T and LWC, respectively (from bottom to height of max LWC) and Γ_{wa} and Γ_{ad} . $\alpha_{eq} = const.$ is defined as deviation from Γ_{ad} which would give the same LWP as original data., which would give the same LWP as the original data.

3.3 Radiometer Data Processing

At the SolarAOT^{upper} station, a CMP21 pyranometer and an Eppley pyrgeometer were installed to measure downwelling shortwave and longwave radiation, respectively. Both instruments recorded data at 42-second intervals. At the SolarAOT_{lower} station, a CNR4 net radiometer was mounted to measure both upward and downward shortwave and longwave fluxes, with a sampling interval of 36 seconds. Data from SolarAOT^{upper} were interpolated to match the temporal resolution of the lower station. Short spikes in the radiometric signal—likely due to transient obstructions such as birds—were removed using a filtering algorithm. Additionally, the signal was smoothed using a 10-minute running mean. The 10-minute averaging window was chosen to correspond to the typical duration of balloon flights (10-15 minutes), allowing for comparison between the measured and simulated radiative fluxes.

3.4 1D Simulations radiation fluxes

Simulations—This section presents the model used to perform optical, microphysical, and radiative closure, as discussed in Section 4.4. The model was used to assess the consistency between observed radiation and retrieved fog microphysical properties. For this purpose, simulations were done in 1D using the Fu-Liou code Fu and Liou (1992, 1993). (Fu and Liou, 1992, 1993)

The Fu-Liou radiative transfer model is a sophisticated tool designed to accurately simulate radiative transfer in the Earth's atmosphere. The Fu-Liou code uses δ -two/four flux approximation, which allows it to efficiently handle the complexities of radiation scattering and absorption by gases, aerosols, and cloud particles. Model covers six short waves—The model covers six shortwave (SW, $\lambda < 4 \mu\text{m}$) and 12 long waves—longwave (LW, Applied spectral bands $\lambda \geq 4 \mu\text{m}$) spectral

bands, making it well-suited for various atmospheric conditions. The Fu-Liou model ~~provide~~provides detailed insights into the interactions between cloud microphysics and radiation. The model vertical levels span from the ground up to 10 km, with a greater density closer to the surface. In the first 100 m, the grid was spaced every 10 m, and from 100 m ~~to~~to 1 km every 100 m. Input ~~to~~into the Fu-Liou model includes profiles of thermodynamic parameters, fog optical and microphysical quantities, aerosol optical properties, and surface reflectance and emissivity.

To perform simulations, the following specific data were provided to the model:

- 365 – T and specific humidity profile. ~~Data from~~The data from the soundings were combined with the sounding from Tarnów (WMO station 12575) - more information is ~~in~~in ~~Appendix~~Appendix given in Appendix A.
- ~~r_{eff}~~r_{eff}; ~~due to limitation of~~Due to limitations of the radiative transfer model; ~~r_{eff} was set~~r_{eff} was set ~~assumed to be~~assumed to be constant with height within the fog ~~the data from OPC-N3 were used to calculate the r_{eff} layer. It was calculated using data from the OPC-N3~~calculate the droplets counts, which measures droplet concentrations in 24 size bins. To ~~calculate r_{eff}~~calculate r_{eff} ~~the bins from~~exclude aerosol particles, only bins 7 ~~till to~~to 24 ~~were used~~were used ~~which corresponds to~~(corresponding to droplet diameters from 1.15 to 20 μm ~~to remove aerosol particles)~~to remove aerosol particles) were used in the calculation.
- ~~fog~~Fog height - in the model was assumed that the fog starts at the surface and ~~reach~~reaches the CTH level. The top of the fog was determined as the point where $\text{LWC} < 0.12 \text{ g}\cdot\text{m}^{-3}$.
- ~~aerosol~~Aerosol optical depth (AOD) - measurements from CIMEL at SolarAOT^{upper} were taken. To adjust how much the beam is weakened by the vertical distance between the upper and lower site; ~~to~~to, the value of AOD was added to the extinction coefficient (obtained from Aurora 4000 and AE-31) times the height difference (185 m) between both stations.
- ~~aerosol~~Aerosol single scattering albedo (SSA) - Based on AE-31 and Aurora 4000 located at SolarAOT^{upper}, the SSA was calculated. The value of SSA at the moment of the balloon sounding was obtained by linear interpolation.
- ~~aerosol~~Aerosol ~~Angstrom exponent~~Ångström Exponent (AE) at 440/870~~nm~~nm. ~~The~~A CIMEL sun photometer is installed at the SolarAOT^{upper} site. For the simulations, AE values were rounded ~~for the simulations to have similar conditions for each simulation, for 8-10 Sep. we assumed AE =~~to ensure consistent conditions across all cases. Data from both CIMEL and lidar indicate an influx of Saharan dust during the period of 8–10 September. The approximate AE value recorded by CIMEL during these days was 0.5 ~~and for~~, increasing to 1.0 on 11 ~~Sep.~~Sep. ~~AE~~September.
- The asymmetry parameter was derived using Mie scattering theory. Initially, the liquid water content and effective droplet radius were employed to estimate the droplet number concentration, assuming a monodisperse size distribution. Subsequently, spectral optical properties—extinction, scattering, and single scattering albedo—were computed across relevant wavelengths. Finally, the asymmetry parameter was calculated by integrating the angular scattering phase function obtained from classical Mie theory.
- The model allows for the specification of surface albedo based on the International Geosphere-Biosphere Program (IGBP) land cover classification, using one of 20 predefined surface types. For all simulations performed in this study, the

IGBP class was set to “grassland” (IGBP = 1.010), as the measurement site was located on a valley slope predominantly covered with grass, with sparse one-family houses. Surface albedo was implemented as a spectrally resolved, solar zenith, and water vapor content dependent parameter.

4 Case study: Valley of Strzyżów city

395 Fog was observed during three successive nights between 8 and 11 September 2023 in the valley of Strzyżów city. The balloon was launched after a fog was visible at the lower station. ~~Apart from apparatus mounted on the balloon, there was at the ground Shadowgraph which was monitoring the LWC, r_{eff} and N_c (Fig. 5 presents the situation at the lower and upper stations during fog occurrence. Fig. 5). The photo A2 presents photographs taken on three consecutive days at 04:00 UTC from the SolarAOT^{upper} station, showing the top of the fog at 4:00 UTC is shown on Fig A2 layer.~~ During the experiment, the fog was
400 not detected at the upper site. The Table 1 presents the duration of each fog and its division into stages. In this section will be described the evolution of each fog as well as its general pattern.

4.1 Meteorological overview

The area of Poland, as well as almost all of Europe, was under the influence of anticyclonic circulation of high pressure from Russia. The pressure on ~~September 9~~ September was constant and it was 1019 hPa, from ~~9 UTC on September~~ UTC on 10
405 September it began to slowly drop to reach the value of 1012 hPa on ~~September 11~~ September at 11 UTC. During days 8-10 September 2023, there was an event of Saharan dust over Poland. The AE measured for those days by CIMEL at SolarAOT^{upper} station ~~where oscillating was~~ around 0.5 (for a period of Saharan dust) and 1.0 (for the morning of 11 September). The mean AOD during the dust episode was not very high (0.19 at 500 nm). ~~The~~ From the lidar data (Fig. A1) can be seen that the sky was mostly cloudless ~~A1, on~~. On September 9 in the morning, cirrus clouds were visible, ~~the~~. The average wind speed did
410 not exceed $2.5 \text{ m}\cdot\text{s}^{-1}$. Slow advection of hot air of tropical origin caused an inflow of Saharan mineral dust visible at 2-4 ~~km~~ km a.g.l. on lidar data A1. The Fig. 5d ~~show~~ shows the aerosol scattering coefficient of light at 525 nm (ASC_{525}), for three nights of observations. On the night between 8-9 September 2023 ASC_{525} was below 100 Mm^{-1} which suggests moderate air quality conditions, just before the onset of fog 21:30-22:30 the values peak to 240 Mm^{-1} and after the end of fog, values once again peak exceed a very high level of 500 Mm^{-1} . These two peaks are probably due to industrial activity during inversion
415 conditions and ~~some turning on the~~ turning on of the heating systems in houses. The morning peak is coincident with inversion disappearance and the transport of pollution from the bottom of the Strzyżów ~~volley~~ valley. On the night between 9 and 10 September the ASC_{525} was descending during the night from 150 to 100 Mm^{-1} , with a peak to 250 Mm^{-1} at 21 UTC. The cleanest conditions, with no evening peak of ASC_{525} , were on night ~~10-11~~ 11 September with values below 100 Mm^{-1} . At the upper station, always in the evening and at night, the values of ASC_{525} were below 100 Mm^{-1} . The air in the valley was
420 trapped under the inversion of temperature. The inversion ~~was starting formed~~ at 18 ~~at the night 08-09 and 09-10:00 at night~~ from days 8 and 9, and around 19 ~~at night 10-11 Sep-:00 at night on day 10, September~~ 2023. The course of T at in the valley each day was similar during the day, reaching a maximum of 24-26 °C, and reaching a minimum 12.5-13.5 °C around 5 UTC

5(Fig. 5). The inversion ~~was disappearing-disappeared~~ around 8:40, 7:40, and 8:10~~respectively-, respectively~~, for days 9, 10, and 11 ~~Sep. September~~ 2023. The RH at SolarAOT~~lower-lower~~ station during fog was reaching 100%. The air at SolarAOT~~upper~~ upper station was lower (RH=60-90%).

The lower panels of Fig. 5 show the calculated visibility in kilometers. Visibility was derived from ShadowGraph measurements using the Koschmieder formula, under the assumption of monodisperse droplets with a radius equal to the r_{eff} obtained from ShadowGraph, and LWC also provided by ShadowGraph data. An extinction coefficient of 2 was assumed, corresponding to the geometrical optics regime.

430 During the nights of 9 and 10 September, visibility decreased sharply around midnight, reaching values as low as 100–200 m. The fog dissipated abruptly around 6:00. In contrast, the fog event on the night of 11 September exhibited a different evolution: intermittent patches of fog began to form around midnight, followed by the development of a more continuous fog layer after 02:00, which persisted until approximately 6:00.

4.2 Fog microphysics

435 Based on OPC-N3 measurements, it was possible to compute LWC and LWP; results for each fog are presented in Fig. 6. Observed fogs were occurring mostly in moderate aerosol conditions, ~~fog layer and fog layers~~ were located in the range of the T inversion. The fog top was varying from sounding to sounding, mostly it was 85 m (max. 115 m) m, see Fig A2-6).

The Fig. 7, ~~Fig-8 and Fig-8~~ and 9 presents the T and RH with height as well as LWC, N_c and r_{eff} for each event of fog. The ~~soundings starts at around~~ profiles are shown starting from 2 m above ~~ground~~the ground, as values below this height could have been significantly affected by surface influence or local disturbances during balloon launch procedures. For this reason, the lines fitted to the profiles were calculated from 2 m to 80% of the fog height. The level of 80% was chosen according to Cermak and Bendix (2011), that above 80% of the height, the fog layer mixes with the dry air above it, which contributes to the reduction of LWC. It is worth ~~to mention-mentioning~~ that at that stage of the year, the sunrise is at 4:00 UTC (local time 6:00). Time is given in UTC; for this period of year, UTC is -2 hours from local time.

4.2.1 Thin-to-thick transition

In the ~~case of observed fogs the possible to check criteria of thin-to-thick transition were: temperature, CTH, and LWP. For Night 08-09 the criteria of LWP~~ observed fog events, several criteria were considered to identify a possible transition from thin to thick fog. Following Costablos et al. (2024), we evaluated: IR net radiation at the surface, temperature, cloud top height, and liquid water path.

450 Costablos et al. (2024) proposed five conditions to characterize this transition: (1) longwave net radiation approaches zero, (2) the temperature gradient between 50 m and 25 m becomes negative, (3) TKE exceeds $0.10 \text{ m}^2 \text{ s}^{-2}$, (4) CTH exceeds 110 m and (5) LWP exceeds 15 g m^{-2} . They demonstrated that while all conditions were met for thick fog, the exact time when each was fulfilled could differ by up to one hour, making precise estimation of the transition time challenging. In this study, we evaluated four out of five conditions proposed by Costablos et al. (2024) (without the TKE condition). The following list outlines which criteria were met during each observed fog event.

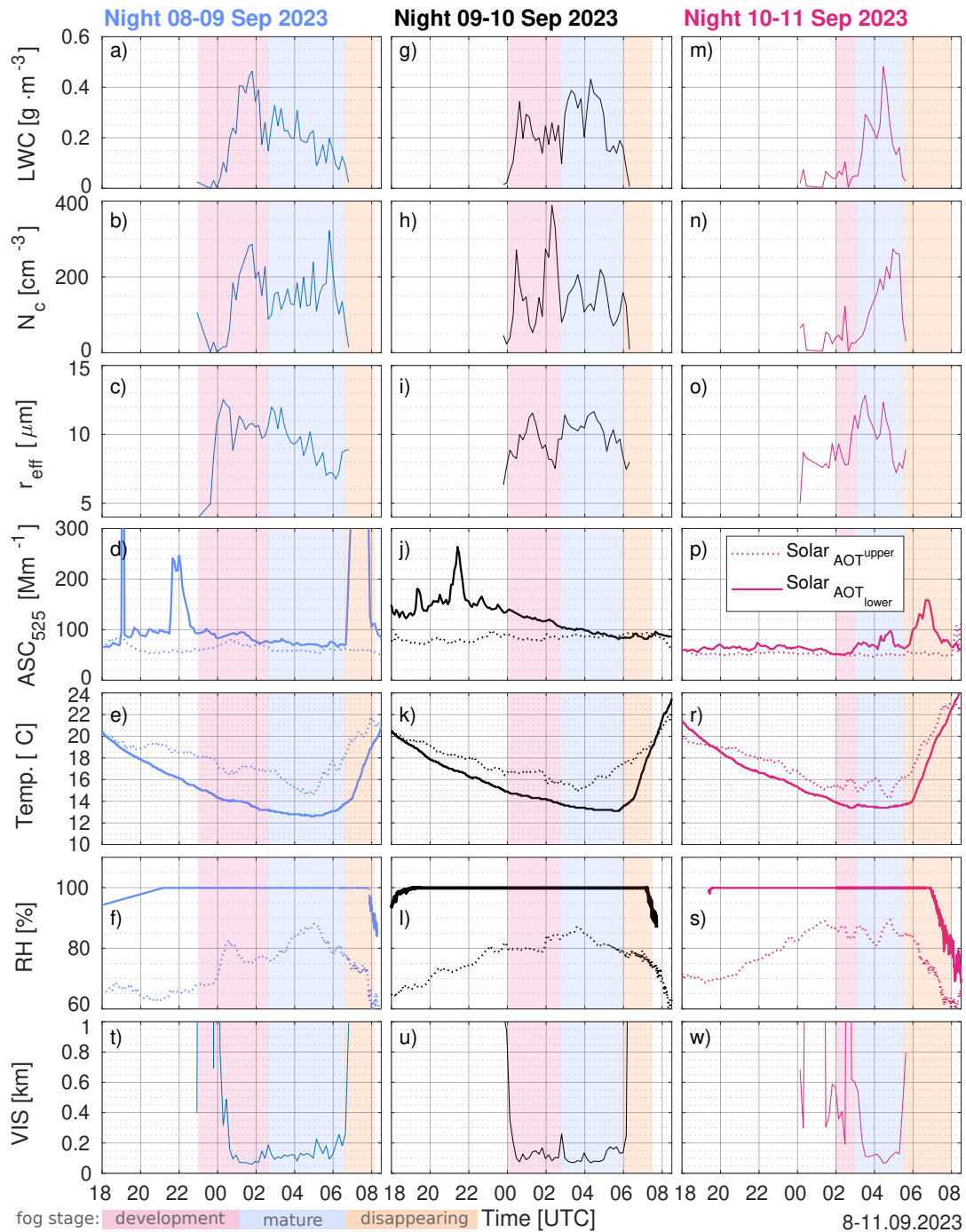


Figure 5. Temporal variability of weather condition on the ground for 09/10/11 September-Sep. 2023 at the SolarAOT~~lower~~^{lower} site (solid lines) and SolarAOT~~upper~~^{upper} station (dotted line). On the panels a), f), g), k) m) is presented by solid line LWC form ShadowGraph, for reference when the soundings of the balloon with installed OPC-N3 occurred an overlay of Fig. 6 was added. Panels b), g), h), h) n) presents the N_c of droplets registered by ShadowGraph. Panels c), h), i), and m) o) shows r_{eff} obtained from ShadowGraph. Figure d), i) j) and n) p) presents the ASC at 525 nm from Aurora 4000; panels e), j), k), o) r) ~~T from MetPak and~~, panels f), l), s) RH and panels t), u), w) visibility obtained from ShadowGraph.

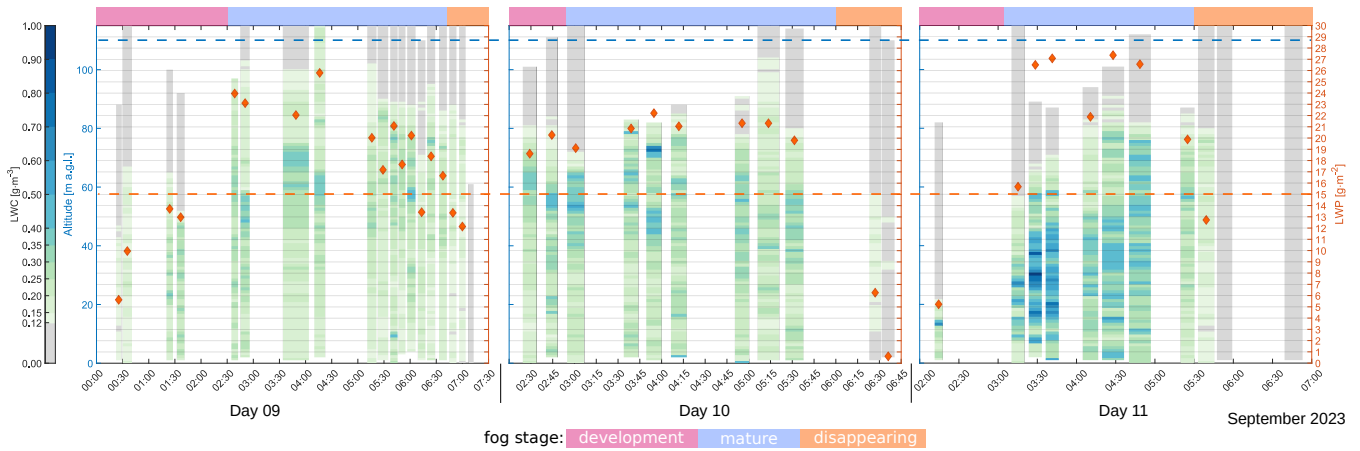


Figure 6. The bar chart with green-blue colors indicates the change in time of fog LWC with height for days a) 09, b) 10, c) 11 Sep. 2023. The left axis represents the height, while the right axis corresponds to the total LWP for each balloon sounding (marked by an orange diamond). Blue dashed line indicates the 110 m, orange line indicates LWP equal to $15 \text{ g}\cdot\text{m}^{-2}$. Those are criteria indicating the transition of fog from thin to thick by (Costablos et al., 2024)

~

460

– On the night of 8–9 September, the LWP exceeded $15 \text{ g}\cdot\text{m}^{-2}$ has been fulfilled at 1:30, the criteria $\text{CTH} > 110 \text{ m}$ at 4:09 (only for one profile). For Night 09–10 the criteria of $\text{LWP} >$ at 01:30. The IR net radiation criterion was satisfied for three profiles at 02:38, 03:48, and 04:16. The profile at 04:16 satisfied three out of the four criteria (IR net radiation, CTH, and LWP) and was conducted during a brief period of thicker fog just before sunrise. However, this state of thick fog did not persist for long.

465

– On the night of 9–10 September, the LWP exceeded $15 \text{ g}\cdot\text{m}^{-2}$ has been fulfilled from the beginning of successful measurements (2 from the start of valid measurements at 02:30), the criteria $\text{CTH} > 110 \text{ m}$ at 5:15 (only for one profile). For Night 10–11 the criteria of $\text{LWP} >$ until the fog dissipated.

– On the night of 10–11 September, the LWP exceeded $15 \text{ g}\cdot\text{m}^{-2}$ has been at 3 at 03:10, the criteria $\text{CTH} >$ but the CTH did not reach the 110 m threshold.

Although the $15 \text{ g}\cdot\text{m}^{-2}$ threshold suggested by Costablos et al. (2024) was frequently exceeded, our results indicate that this value alone is insufficient to reliably distinguish between thin and thick fog. Therefore, we interpret the fog event on 9 September as a case in which a transition towards thick fog had started but was interrupted by sunrise before full development. In the fog events on 10 and 11 September, the other criteria were not met.

470

In none of fog occurrence LWP exceeded these cases did the LWP exceed $30 \text{ g}\cdot\text{m}^{-2}$ as proposed by Wærsted et al. (2017). In our opinion as most of the criteria were not fulfilled, we think the proposed adjustment of LWP criteria by Costablos et al. (2024) is too weak in our case. In our understanding none of the cases transitioned to thick fog — the threshold for thick fog proposed

by Wærsted et al. (2017). Given that the period of thick fog was very short-lived and most observations remained within the thin fog regime, our findings should be considered primarily representative of optically thin fog conditions.

475 4.2.2 Night 08-09 Sep. September 2023

The fog on Night 08-09 Sep. event during the night of 8- 9 September 2023 was captured from the development state observed from its development stage (23:00–100–01:41UTC), through grown state (2:45–6) its mature stage (02:45–06:42UTC) till disappearing (6:45–7), until dissipation (06:45–07:00UTC). Fig. 7 presents the profiles of microphysics parameters such as vertical profiles of microphysical parameters, including LWC, N_c and r_{eff} , as well as atmospheric along with T and RH (the division for each stage is plotted in the Appendix Fig. A3a, Fig. A3b, Fig. A3c).

Costablos et al. (2024) compares the registered profiles of LWC with the proposed theoretical profiles of LWC by Toledo et al. (2021). The proposed conceptual model of fog was introduced in Sec. 3.2, the equivalent adiabaticity α_{eq} is added on the figures presenting LWC.

In obtained profiles it is visible strong influence of ground to the profiles of LWC, T near the ground. Therefore, apart from α_{eq} to LWC a straight line was fitted from the 2-m to height of maximum LWC. In this way, the adiabatic profile scaling factor LWC was obtained α_{Tt} , similarly as in the article Costablos et al. (2024). According to the assumption by Cermak and Bendix (2011), above 80% of the height, the fog layer mixes with the dry air above it, which contributes to the reduction of LWC.

Based on measurements with OPC-N3 it was possible to compute LWC and LWP which are presented on. The equivalent adiabaticity (α_{eq}) is shown in the figures displaying LWC profiles. The division into fog life cycle stages is illustrated in Fig. 7 by pink, blue, and yellow ochre corresponding to the development, mature, and dissipation stages, respectively. Apart from that, separate figures can be found in the Appendix for each stage: Fig. 6. At 3 m above ground was mounted Shadowgraph which was constantly monitoring LWC during each episode (see A3a, Fig. A3b, and Fig. 5).

On the left axis changes of fog LWC with height for a) 09, b) 10, c) 11 September 2023. On the right axis is total fog LWP for each balloon sounding. Blue dashed line indicates the 110 m, orange line indicates LWP equal to 15 g m^{-2} . Those are criteria indicating the transition of fog from thin to thick by Costablos et al. (2024).

Vertical profiles of specific quantities measured by the balloon for night night 08-09 September 2023. From left: T and RH from Vaisala radiosonde RS41, LWC, N_c , r_{eff} within the fog from OPC-N3. Each colored line represents one balloon profile. Black thick line represents the mean of all the soundings, colored area represents range in between +/- standard deviation from the mean. On the r_{eff} plot the red line indicates the linear fit to the data. On the N_c plot the yellow line indicates the quadratic fit to the data. At the T plot dotted line presents the adiabatic lapse rate, dashed red line presents the linear fit to T from 3 m to height of maximum mean LWC. At the LWC plot dotted line presents the LWC adiabatic lapse rate, dashed red line presents the linear fit to LWC from 3 m to height of maximum mean LWC. Each of A3c. Each of the fog stages is described below.

– **Development of fog:** There were done 5 soundings conducted between 23:00–200–2:34 (see Fig. A3a). The T was decreasing with height from the ground to 40 m a.g.l. Starting, starting from T = 12.0 °C and decreasing at the rate

$\gamma_{fit} \cdot \Gamma_{wa} = 0.48 \cdot (-5.0)^\circ\text{C} \cdot \text{km}^{-1}$. Above 40 m ~~was the inversion~~, a temperature inversion was present, with T reaching 14.7 °C at 100 m. The top of the fog was 65 m. The RH was constant ~~equal~~, equal to 100% till up to 87 m, and in the last 10 m ~~drooping it dropped~~ with height (96% at 100 m). LWC was slightly ~~growing increasing~~ with height (~~$\alpha_{fit} \cdot \Gamma_{ad} = 1.34 \cdot 2.32$~~ $\alpha_{fit} \cdot \Gamma_{ad} = 1.34 \cdot 2.32$ $\text{g} \cdot \text{m}^{-3} \cdot \text{km}^{-1}$), from 0.18 to ~~maximum a maximum of~~ 0.30 $\text{g} \cdot \text{m}^{-3}$ at 23 m a.g.l., ~~till~~; up to 36 m a.g.l., LWC was oscillating near ~~value~~ 0.26 $\text{g} \cdot \text{m}^{-3}$, ~~an above decreasing to CTH and above that it decreased~~. The α_{eq} was 0.29. The $\text{LWC}_{\text{ShadowGraph}}$ (referring to LWC measured by ~~ShadowGraph mounted 3 m a.g.l.~~) ~~(the ShadowGraph, Fig. 5) show that in the developing stages shows that during the development stage, LWC_{ShadowGraph} was fast increasing to reach its maximum increased, reaching its maximum of 0.46 $\text{g} \cdot \text{m}^{-3}$ at 1:47. Values of LWC from ShadowGraph are higher than were higher than those from OPC-N3. The LWP (Fig. 6) grow increased from 5.63 $\text{g} \cdot \text{m}^{-2}$ at 00:25 to 12.97 $\text{g} \cdot \text{m}^{-2}$ at 1:36. Mean N_c was growing increased with height to 247 cm^{-3} at a 35 m. Than decreasing, then decreased with height to 48 cm^{-3} at 65 m. The r_{eff} was constantly decreasing ~~eff~~ decreased steadily with height from 11.2 to 5.7 μm at the CTH.~~

– **Mature state of fog:** There were ~~done~~ 13 soundings conducted from 2:34 till 6:42 (Fig. A3b). The T and RH ~~have showed a~~ similar pattern with height as in the previous stage. The fog ~~deepen, it top was was deeper, with a top~~ at 102 m. However ~~the inversion of temperature starts~~, the temperature inversion started higher, around 60 m above the ground, and the ~~lower part lapse rate is higher~~ lapse rate in the lower part was higher: $\gamma_{fit} \cdot \Gamma_{wa} = 1.16 \cdot (-5.1)^\circ\text{C} \cdot \text{km}^{-1}$. The N_c maximum, equal to 410 cm^{-3} , was at 48 m, ~~above the~~; above this, N_c ~~decreases up~~ decreased to 65 cm^{-3} at 90 m. Above that, the number of drops was constant. The r_{eff} profile ~~has changed~~, it changed and can be divided into two areas sections. From the ground to a height of 88 m, r_{eff} ~~it is remained~~ almost constant (at bottom 9.2 μm ; 8.3 μm at 88 m). From 88 m to CTH ~~the~~, r_{eff} decreased with height sharply sharply with height (mean at the top 5.2 μm). Because the N_c maximum ~~shifted upper also is shifted upward, the~~ LWC maximum is also at a higher altitude (56 m). The α_{fit} is positive, equal to 0.90, and α_{eq} is equal to 0.30. The ~~picture images~~ from the ShadowGraph ~~shows indicate~~ that $\text{LWC}_{\text{ShadowGraph}}$ near the ground ~~was decreasing in time~~ decreased over time starting from 2:57 ~~and this fact~~, and this was associated with a decrease in r_{eff} and not N_c .

– **Disappearing phasestage:** There were ~~conducted~~ 2 soundings in conducted between 6:45 and 7:00 (Fig. A3c). The T ~~is growing from~~ increased from the ground to 27 m, above ~~T is decreasing which T decreased~~ with height. Unfortunately, the sounding with the Vaisala radiosonde RS41 was interrupted at 45 m. Between ~~two soundings spaced apart by the two soundings, spaced~~ less than 15 minutes apart, the T profile shifted by +2 °C. In this time At this time, the RH profile ~~drooped dropped~~ by 5%. In the first 20 m, the mean RH ~~drooped dropped~~ from 96 % near the ground to 91% at 20 m. ~~Fog~~ The fog evaporated quickly. The α_{eq} was positive, equal to 0.33. LWC ~~was rising~~ increased with height (~~$\alpha_{fit} \cdot \Gamma_{ad} = 0.42 \cdot 2.39$~~ $\alpha_{fit} \cdot \Gamma_{ad} = 0.42 \cdot 2.39$ $\text{g} \cdot \text{m}^{-3} \cdot \text{km}^{-1}$) ~~reaching~~, reaching a maximum at 72 m (mean LWC 0.26 $\text{g} \cdot \text{m}^{-3}$) ~~also~~; at almost the same height ~~the~~, N_c ~~has also reached~~ its maximum (488 cm^{-3} at 74 m). The layer above ~~is characterize by rapid droop of both values to~~ was characterized by a rapid decrease in both values up to the CTH. The r_{eff} was constant with

540 height up to 80 m, around $6.8 \mu\text{m}$, ~~apart from layer from except for the layer from the~~ ground to 18 ~~mm~~, where r_{eff} was ~~grater higher~~, up to $9.5 \mu\text{m}$.

The Fig. 7 ~~shows presents~~ the mean values with height for the ~~whole night whole-night~~ fog event from 08-09 ~~Sep. September~~ 2023. For the ~~whole fog evententire fog event~~, α_{eq} is 0.23. ~~The first approximationof~~ ~~As a first approximation~~, fog r_{eff} ~~is a~~ ~~linear decrease with heightdecreases linearly with height~~, while N_c can be ~~fitted with approximated by~~ a quadratic equation. ~~The equations for fitted lines are respectively:~~

545
$$N_c r_{\text{eff}} = -0.10 \cdot h^2 \cdot 10 + 8.270.03 \cdot h + 130.249.06 [\text{cm}^{-3} \mu\text{m}], \quad (11)$$

$$r_{\text{eff}} N_c = 3.00 - 0.10 \cdot h^2 \cdot 10^{-2} + 9.068.27 \cdot h + 130.24 [\mu\text{m cm}^{-3}]. \quad (12)$$

4.2.3 Night 09-10 ~~Sep. September~~ 2023

Below are described the ~~phases stages~~ of fog from ~~09-10 Sep. 202309- 10 September 2023~~:

550 – **Development of fog:** Due to ~~malfunctioning a malfunction~~ of the apparatus ~~the development of fog stage~~, ~~the development~~ ~~stage of fog~~ with microphysics measurements in ~~vertical were the vertical direction was~~ not captured. The fog started at 00:00, ~~howeverit~~; ~~however, it is~~ not possible to determine when this stage ended. The first OPC-N3 ~~registered sounding~~ ~~was sounding was registered~~ at 2:34, with $\text{LWP} > 15 \text{ g} \cdot \text{m}^{-2}$. ~~Based on measurements with Shadowgraph the LWC,~~ ~~Based on ShadowGraph measurements, LWC and N_c~~ , ~~grow constantly to increased continuously until 00:37~~ ~~reaching~~ ~~local maximum of~~, ~~reaching local maxima:~~ $\text{LWC}_{\text{ShadowGraph}} = 0.34 \text{ g} \cdot \text{m}^{-3}$ and $N_c = 271 \text{ cm}^{-3}$. The r_{eff} reached its local maximum later, at 1:17, equal to $11.6 \mu\text{m}$. After the peak, values of LWC, N_c , and r_{eff} ~~were fluctuating reaching its~~ ~~global maxima fluctuated, reaching their global maxima~~ ($N_c = 388 \text{ cm}^{-3}$ ~~cm⁻³~~ at 2:18 ~~and minima~~) and minima ($r_{\text{eff}} = 7.5 \mu\text{m}$ at 2:28. ~~There were done two 28~~).

560 ~~Two profiles of T and RH~~, ~~shown on are shown in~~ Fig. A4a. ~~Profile reaching~~ ~~The profile reaching~~ a higher altitude was ~~done earlier performed earlier~~, at 00:53 ~~and other was done after one hour~~. ~~Profile of T was almost constant in~~, ~~and the~~ ~~second about one hour later~~. The temperature profile was nearly constant in the first 40 m ($12.65 \text{ }^\circ\text{C}$ at the ground), above ~~was inversion of T which with time weakened~~ ~~which a temperature inversion was present that weakened with time~~. The RH was 100% ~~till % up to 67 m~~, ~~above decreasing then decreased~~ with height. ~~However, one hour later the~~ ~~One hour~~ ~~later~~, RH was constant at 100% ~~in the whole column from ground % throughout the entire column from the ground up~~ to 86 m.

565 – **Mature state of fog:** There were ~~done~~ 13 soundings ~~conducted~~ from 2:45 ~~till to~~ 6:42 (Fig. A4b). The fog height was 87 m. The ~~T was decreasing with height till~~ ~~temperature decreased with height up to~~ 50 m a.g.l., above ~~was inversion~~ ~~of T~~. ~~From ground till the CTH~~ ~~the RH was~~ ~~which a temperature inversion occurred~~. ~~From the ground to the CTH,~~

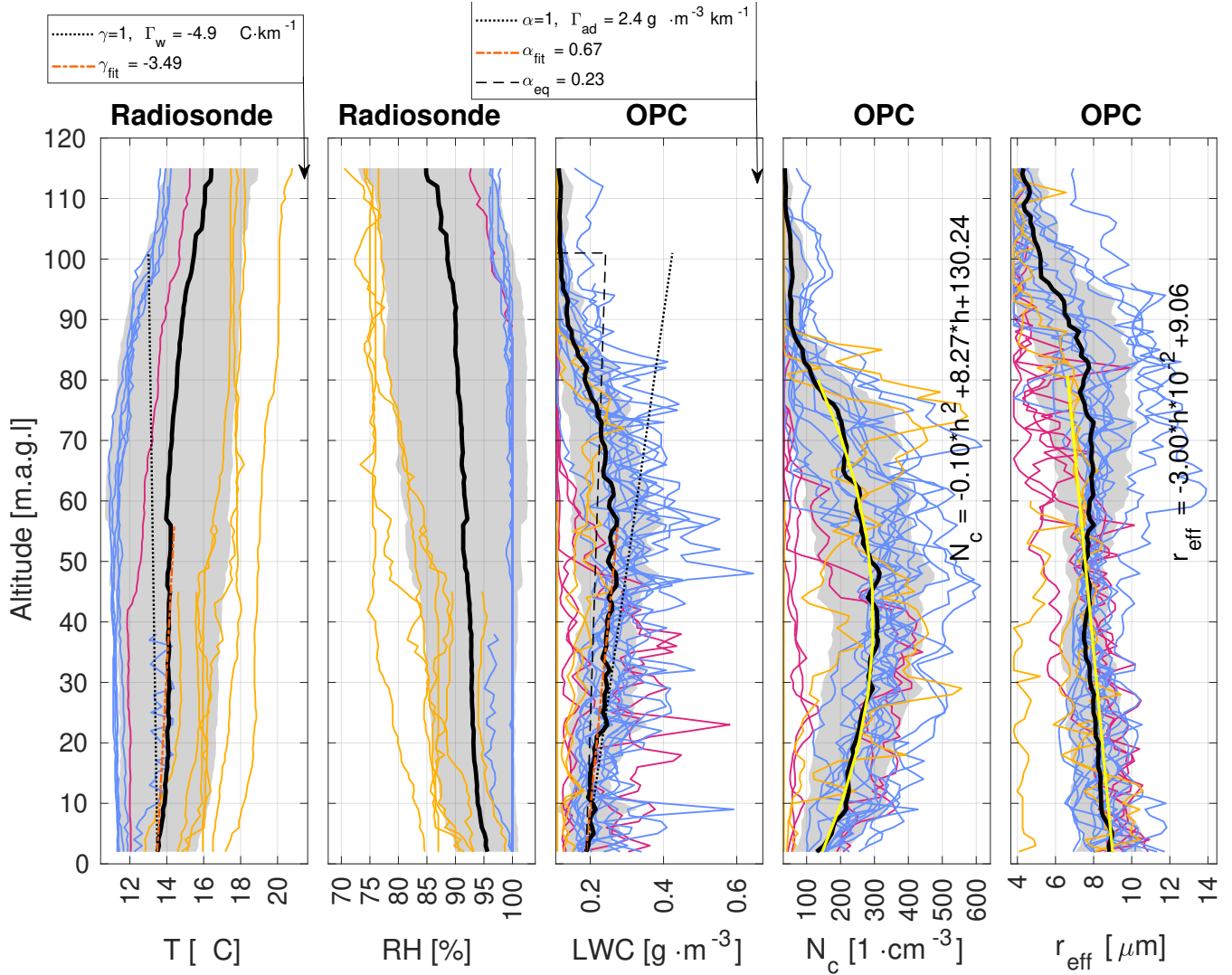


Figure 7. Vertical profiles of specific quantities measured by the balloon for night 08-09 Sep. 2023. From left: T and RH from Vaisala radiosonde RS41, LWC, N_c , r_{eff} within the fog from OPC-N3. Each colored line represents an individual balloon profile, with different colors indicating different stages of fog evolution: pink corresponds to the formation stage, blue to the mature stage, and yellow ochre to the dissipation stage. The black thick line represents the mean of all the soundings, the colored area represents the range between \pm standard deviation from the mean. At the T plot dotted line presents the wet adiabatic lapse rate Γ_w , dashed red line presents linear fit of T from 2 m to height of maximum mean LWC. γ_{fit} is a scaling factor of Γ_w to obtain the equation of linear fit. At the LWC plot dotted line presents the LWC adiabatic lapse rate Γ_{ad} , the dashed red line presents the linear fit to LWC from 2 m to the height of maximum mean LWC. Where α_{fit} is a scaling factor of Γ_{ad} obtained by fitting line to LWC dependence from height and α_{eq} is a scaling of Γ_{ad} which would give the same LWP for the whole cloud/fog. On the N_c plot, the yellow line indicates the quadratic fit to the data (from 2 m to 80% height of CTH). On the r_{eff} plot the yellow line indicates the linear fit to the data (from 2 m to 80% height of CTH).

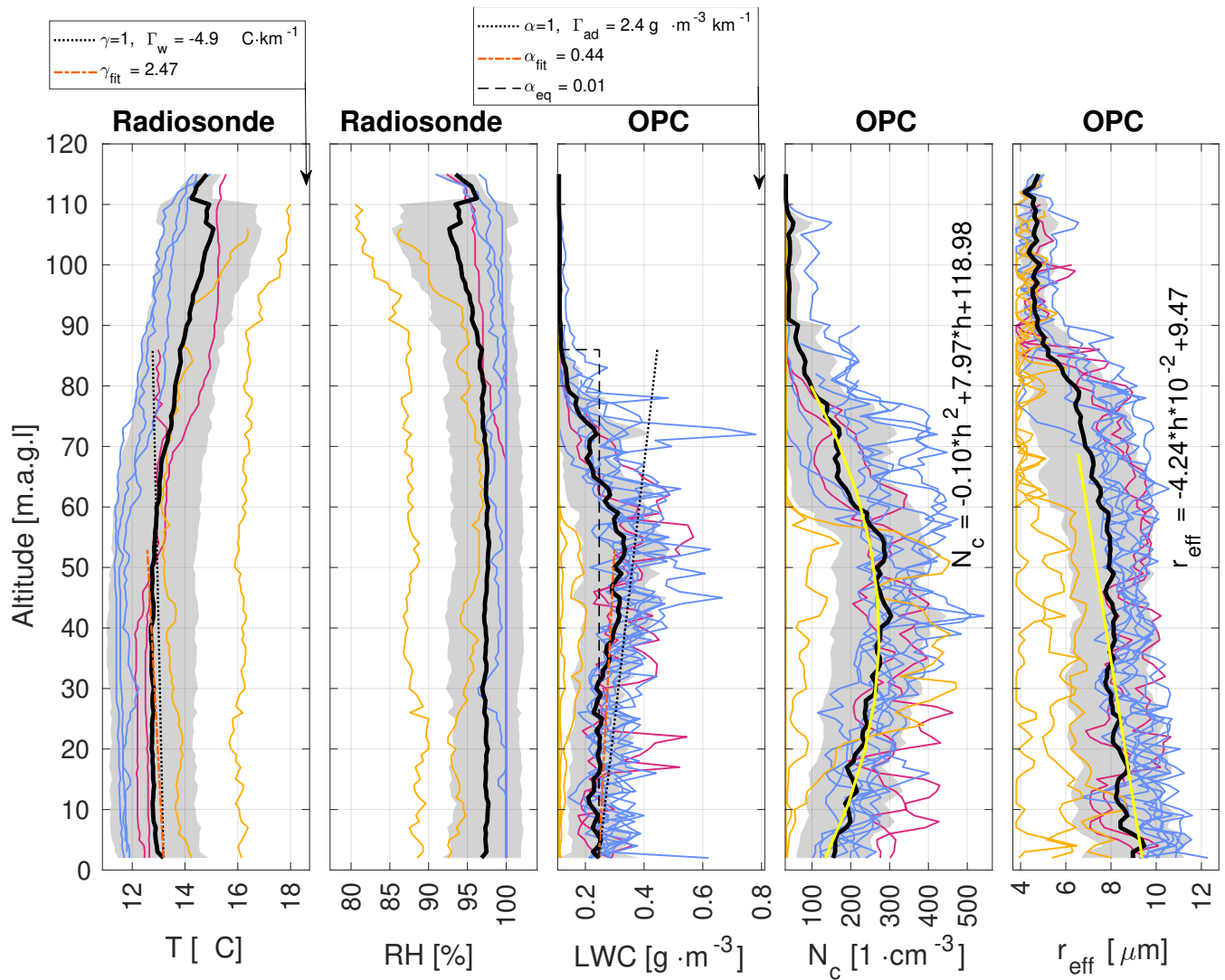


Figure 8. Vertical profiles of specific quantities measured by the balloon for night **night**09-10 September 2023. The detailed description is given in [the caption of Fig. 7](#).

RH remained above 99.5%. **Maximum-LWC** was ~~The maximum LWC was observed~~ at 53 m, **LWC** = ~~with a value of~~ 0.40 g·m⁻³. ~~To LWC~~

A linear fit to the LWC profile from 2 m to 53 m ~~was fitted line with growing~~ yielded a growth rate equal to 0.51 of the LWC adiabatic lapse rate. ~~There max~~ ~~The maximum~~ **N_c** was lower ~~then in previous night~~ than during the previous night, ~~reaching~~ 345 ~~cm⁻³cm⁻³~~. The **r_{eff}** at the ground was higher than in ~~previous day fog, however~~ the **r_{eff}** was ~~decreasing the~~ ~~previous day's fog; however, it decreased~~ with height in the first 30 m, ~~remained approximately constant~~ (9.0 μm) from

570

575 30 to 63 m ~~was constant approx. $9.0 \mu\text{m}$ and later decaying with height to CTH.~~, and then decreased again toward the CTH.

The LWP (Fig. 6) ~~was oscillating between 18-23~~ oscillated between 18 and 23 $\text{g}\cdot\text{m}^{-2}$. Most of the water was located in the upper part of the fog, between 30 and 70 m.

– **Disappearing phase stage:** ~~There were conducted 5 soundings in~~ Five soundings were conducted between 6:30 and 7:30 UTC (Fig. -A4c). The ~~T at the temperature at~~ 2 m a.g.l. and ~~in the whole column was fast rising throughout the column~~ increased rapidly (from 11.9 °C at 6:30 to 16.22 °C at 7:30. ~~The T in 30).~~ In the first 54 m ~~was decaying~~, T decreased with height, and ~~higher there was an inversion of T~~ above this level, a temperature inversion was observed. As the sun rose, ~~the RH value~~ RH decreased from 100% to 88% at 2 m ~~above the ground a.g.l.~~

585 The parameters α_{fit} ~~was 0.30~~ and α_{eq} ~~was were 0.30 and 0.24.~~ ~~The values of LWC,~~ respectively, LWC values were below 0.12 ~~in $\text{g}\cdot\text{m}^{-3}$ in the~~ first 21 m above ground, ~~maximum LWC = the ground.~~ The maximum LWC (0.15 ~~was $\text{g}\cdot\text{m}^{-3}$)~~ occurred at 43 m. When fog almost ~~disappear dissipated~~ (6:23 UTC, Fig. 6) ~~there where,~~ remaining fog patches at levels from 30-50 ~~were still observed between 30 and 50 m,~~ where LWC was above with $\text{LWC} > 0.15 \text{ g}\cdot\text{m}^{-3}$. The fog peak fell to a height of ~~top dropped to~~ 57 m.

590 Fog droplet diameter ~~was decaying decreased~~ with height from 6.7 μm at 4 m ~~above ground a.g.l.~~ to 4.8 μm at CTH. ~~The the CTH.~~ N_c ~~was oscillating around value~~ fluctuated around 170 cm^{-3} between 24 m and 56 m. The fog was ~~disappearing from both above and below~~ dissipated from both the top and bottom.

The ~~T temperature~~ in the first 53 m was almost constant with height. ~~In this layer the LWC was increasing~~ Within this layer, LWC increased with height at ~~rate $\alpha_{fit} \cdot \Gamma_{ad} = 0.44 \cdot 2.4$ a rate of $\alpha_{fit} \cdot \Gamma_{ad} = 0.44 \cdot 2.4 \text{ g}\cdot\text{m}^{-3}\cdot\text{km}^{-1}$)~~ reaching local maximum, reaching a local maximum of $\text{LWC} = 0.33 \text{ g}\cdot\text{m}^{-3}$ at 53 m. The ~~corresponding~~ value of α_{eq} was ~~almost zero (0.01).~~ nearly zero (0.01).

595 Fig. 8 ~~summaries summarizes~~ the microphysical properties of ~~fog event at the fog event on~~ 09-10 Sep. ~~September~~ 2023. ~~To~~ The following curves were fitted to the values of N_c and r_{eff} ~~were fitted following curves:~~

$$N_c = -0.10 \cdot h^2 \cdot 10 + 7.97 \cdot h + 118.98 [\text{cm}^{-3}], \quad (13)$$

600 $r_{eff} = 4.29 \cdot h \cdot 10^{-2} + 9.47 [\mu\text{m}], \quad (14)$

4.2.4 Night 10-11 Sep. ~~September~~ 2023

The fog pattern on ~~night the night of~~ 10-11 Sep. ~~look different~~ ~~September looks distinct~~ from previous nights. The fog could not form until 3:08, when it started to develop with an abrupt jump in LWC from 0.05 at 3:08 to 0.30 at 3:31 UTC, ~~the 31.~~ The maximum peak in LWC observed on the ground by ShadowGraph was at 4:27 UTC, equal to 0.48 $\text{g}\cdot\text{m}^{-3}$. ~~With fast~~ growth ~~Fog rapidly intensified~~, reaching high LWC values (mean 0.48 $\text{g}\cdot\text{m}^{-3}$) in the fog body from 10-50 m, with maximum

LWC $0.97 \text{ g}\cdot\text{m}^{-3}$ at 31 m at 3:23 UTC. At 4:40 UTC, high values of LWC above $0.40 \text{ g}\cdot\text{m}^{-3}$ were distributed in the range from the fog bottom to 80 m above. As it quickly appeared it also quickly disappeared. As quickly as it appeared, the fog dissipated by 5:40 UTC. However, as before, the fog was more vanishing from dissipating more from the bottom than from the top.

610 During the night of 10-11 Sep. September 2023 all phases, all stages of fog were captured, below; each stage is described in detail. This event of fog below. This fog event developed later in the night than previous cases and it had exhibited more abrupt behavior.

– **Development of fog:** Between midnight and 2:28, the ShadowGraph was detecting droplets however; however, the LWC_{ShadowGraph} was below $0.1 \text{ g}\cdot\text{m}^{-3}$. There were performed two soundings. Two soundings were performed, one with OPC-N3 and one with the Vaisala radiosonde RS41, between 2:00 and 3:02 (Fig. A5a). The profile from 2:11 shows that the fog was just forming. LWP was $5.23 \text{ g}\cdot\text{m}^{-2}$.

Fog was confined to the first 23 m in height. Even though the fog was shallow it at some levels, it had high LWC values at some levels (max. LWC was $0.67 \text{ g}\cdot\text{m}^{-3}$ at 13 m). The $\alpha_{eq} = -3.22$, however $\alpha_{fit} = -0.15$. $\alpha_{eq} = -3.22$, however $\alpha_{fit} = -0.15$.

620 The fog was dense maximum N_c was 416 cm^{-3} at 18 m. The r_{eff} was decreasing with height ($9.8 \mu\text{m}$ at 2 m and $6.0 \mu\text{m}$ at the CTH). The profile from the Vaisala radiosonde RS41 at 2:43 shows that the T was T remained almost constant in the first 40 m (around $12.7\text{--}12.8 \text{ }^\circ\text{C}$), later slightly increasing with height to $14.2 \text{ }^\circ\text{C}$ at 100 m. The profile of RH

The RH profile was constant with height, however, however, the air was not fully saturated, RH was around ($\text{RH} \approx 98.5\%$). ShadowGraph show that LWC dropped. ShadowGraph shows that LWC dropped to 0 at 2:38 and in, and within the next hour fast rebuild LWC to value, rapidly rebuilt to $0.30 \text{ g}\cdot\text{m}^{-3}$. This was correlated with fast growing rapid growth of r_{eff} from $7.8 \mu\text{m}$ to $12.8 \mu\text{m}$, as while N_c was at low value remained low ($2\text{--}65 \text{ cm}^{-3}$).

– **Mature state of fog:** Between 3:10 and 5:30 was conducted 8 soundings with, eight soundings with a balloon (Fig. A5b) were conducted. The fog deepened deepened to 83 m. Profile The profiles of T and RH has changed. Only changed: only in the first 10 m the RH was was RH above 99.5% . Above was decreasing with height, above which it decreased to 85.5% at 60 m. Unfortunately

Unfortunately, the sounding with the Vaisala radiosonde RS41 did not reach the CTH. There was a strong inversion, the fitted lapse rate was $\gamma_{fit} \cdot \Gamma_{wa} = -11.82 \cdot -4.97 \text{ }^\circ\text{C}\cdot\text{km}^{-1}$. The T was increasing T increased from $12.3 \text{ }^\circ\text{C}$ at the ground to $15.8 \text{ }^\circ\text{C}$ at 60 m. The profile of

635 The N_c has different form than in profile had a different form compared to previous fog events, it consists of: it exhibited two protrusions with a maximum maxima at 25 m (377 cm^{-3}) and 70 m (257 cm^{-3}), and a decrease in the number of drops at a height of local minimum at 50 m. The r_{eff} is slightly decreasing in the layer from slightly decreased from the

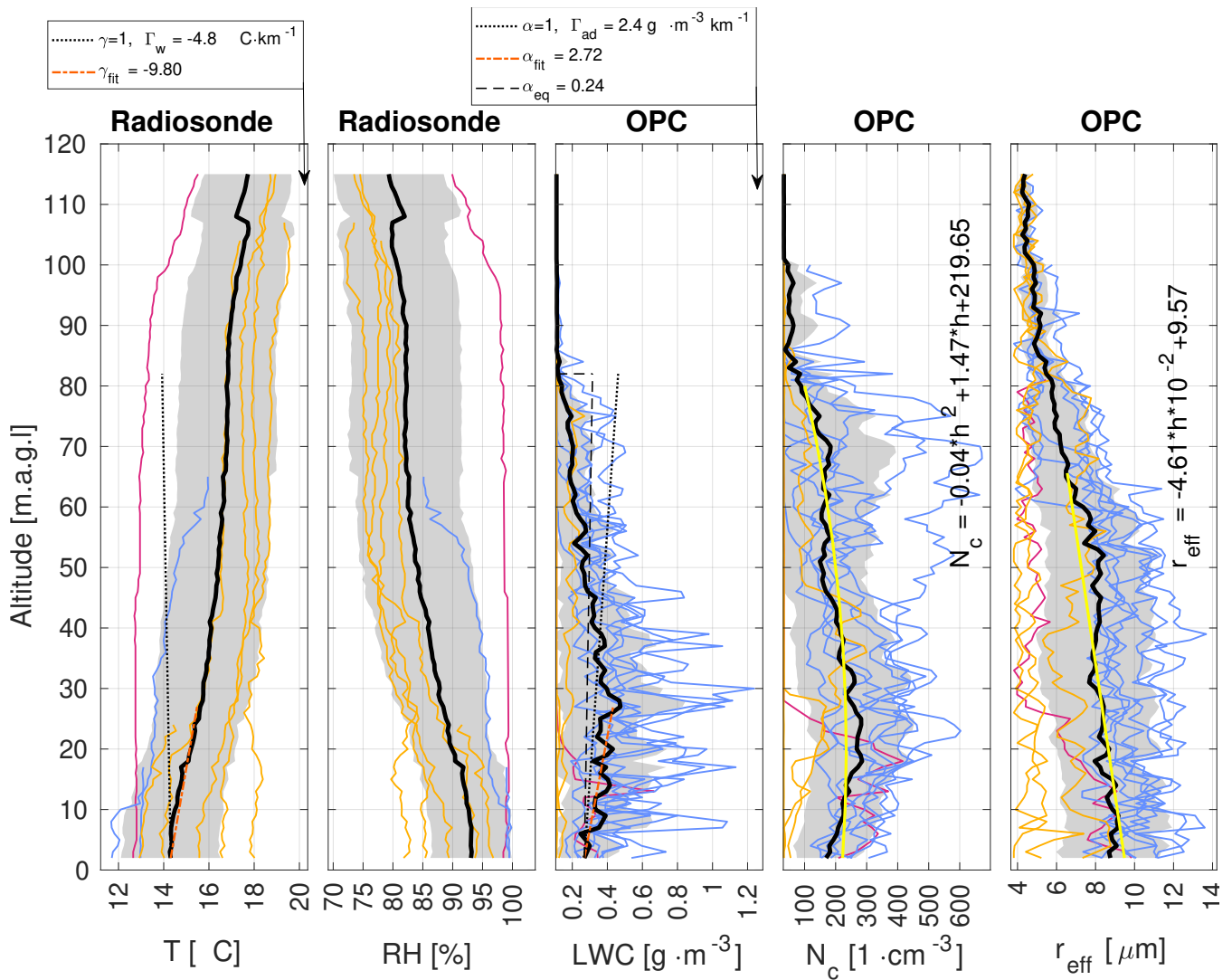


Figure 9. Vertical profiles of specific quantities measured by the balloon for the night of 10-11 September 2023. The detailed description is given in the caption of Fig. 7.

ground ($10.0 \mu\text{m}$) to 60 m ($8.8 \mu\text{m}$). From 60 m to CTH the r_{eff} decreases with height more abruptly, then decreased more sharply to $5.5 \mu\text{m}$ at CTH. Profile of LWC shows the CTH.

640

The LWC profile showed a more intermittent pattern with values highly fluctuating from, with values fluctuating between 0.2 to and $1.2 \text{ g} \cdot \text{m}^{-3}$ having a peak at 27 m equal to and a peak of $0.67 \text{ g} \cdot \text{m}^{-3}$. The $\alpha_{\text{eq}} = 0.56$ and fitted $\alpha_{\text{fit}} = 4.80$ at 27 m. The $\alpha_{\text{eq}} = 0.56$, and the fitted $\alpha_{\text{fit}} = 4.80$. The LWP was the highest from of all three events, for four soundings LWP was above, LWP exceeded $26.5 \text{ g} \cdot \text{m}^{-2}$ (maximum; $27.36 \text{ g} \cdot \text{m}^{-2}$ at 4:27).

– **Disappearing phasestage:** The ~~last-phase final stage~~ of fog was observed from 5:30 to 6:00, ~~there were done 2 soundings~~
 645 ~~00. Two soundings were conducted~~ with OPC-N3, ~~in the~~. In Fig. A5 ~~are also included two~~, two additional soundings
 of T and RH between 6:00 and 6:33. ~~33 are also shown~~. The CTH was at 79 m. ~~The LWC was growing~~
~~LWC increased~~ with height, ~~maximum LWC was almost at with a maximum near~~ the CTH (max. LWC = 0.19 g·m⁻³ at
 75 m). ~~Because of location of max. LWC near CTH the $\alpha_{eq} = 0.32$~~ ~~Due to the location of the maximum LWC near the~~
~~CTH, $\alpha_{eq} = 0.32$, which~~ was similar to ~~$\alpha_{fit} = 0.30$~~ . ~~The $\alpha_{fit} = 0.30$~~
 650 ~~N_c was increasing increased~~ with height to 27 m ~~where it had~~ (maximum 190 cm⁻³, ~~and then oscillating~~), ~~then oscillated~~
 around 145 cm⁻³ ~~till up to~~ 43 m ~~above ground~~, and sharply ~~decreasing decreased~~ to 62 cm⁻³ at 48 m. The r_{eff} ~~was slightly~~
~~decreasing slightly decreased~~ with height, with fluctuations around 6 μm .

Fig. 9 ~~summarize summarizes~~ the microphysical properties of ~~fog event at the fog event on~~ 10-11 ~~Sep-September~~ 2023. The
 α_{eq} for the ~~whole-entire~~ event was 0.24. ~~To~~ ~~The following curves were fitted to the~~ values of N_c and r_{eff} ~~were fitted following~~
 655 ~~curves~~:

$$N_c = -0.04 \cdot h^2 \cdot 10 + 1.47 \cdot h + 219.65 \text{ [cm}^{-3}\text{]}, \quad (15)$$

$$r_{eff} = 4.61 \cdot h \cdot 10^{-2} + 9.57 \text{ [}\mu\text{m]}. \quad (16)$$

4.3 Evolution of fog droplet spectrum

660 ~~The~~ ~~From the~~ OPC-N3 ~~measures droplets in 24 bins, therefore measurements~~, it was possible to compute vDSD(r) presented ~~at~~
~~in the~~ Fig. 11 a). The vDSD is presented from bins of radius from 1.15 to 20 μm to remove aerosol particles. ~~Near the ground~~
~~was located ShadowGraph~~, Figure 10 presents the comparison between the vDSD obtained from ShadowGraph and OPC-N3. ~~ShadowGraph~~
~~shows that near the ground, there are droplets of radius greater than 20 μm , and that in the case of OPC-N3,~~
~~those droplets are counted in the last bin~~. As it was stated by Nurowska et al. (2023) ~~even though manufacturer declare~~, ~~even~~
 665 ~~though the manufacturer declares~~ that the upper limit of the last bin is 20 μm , in fact, ~~the last bin also counts larger particles~~.

~~The obtained vDSD was not calibrated with ShadowGraph. Vertical profile of vDSD gives information which droplets give biggest contribution to LWC at specific height. Apart from vDSD at Fig. 11 on panel~~

~~Although OPC-N3 is not calibrated to match the vDSD values, it has a similar pattern of spectrum as ShadowGraph. The vertical profile of the vDSD (Fig. 11a) provides information on which droplet sizes contribute most to the LWC at a given~~
 670 ~~height. Figure 11b) is shown vDSD with normalization. Normalization consists of dividing the whole spectrum at a given~~
~~shows the normalized vDSD, obtained by dividing the droplet size distribution at each height by $\sum_{r_b} \text{vDSD}(r_b)$ from a given~~
~~height. In this way, Fig. 11 b) shows what percentage of the entire spectrum at that height. This normalization highlights the~~
~~relative contribution of each size bin to the vDSD at a given height is contributed by the volume of drops from a given bin. Fig.~~
~~11 altitude.~~

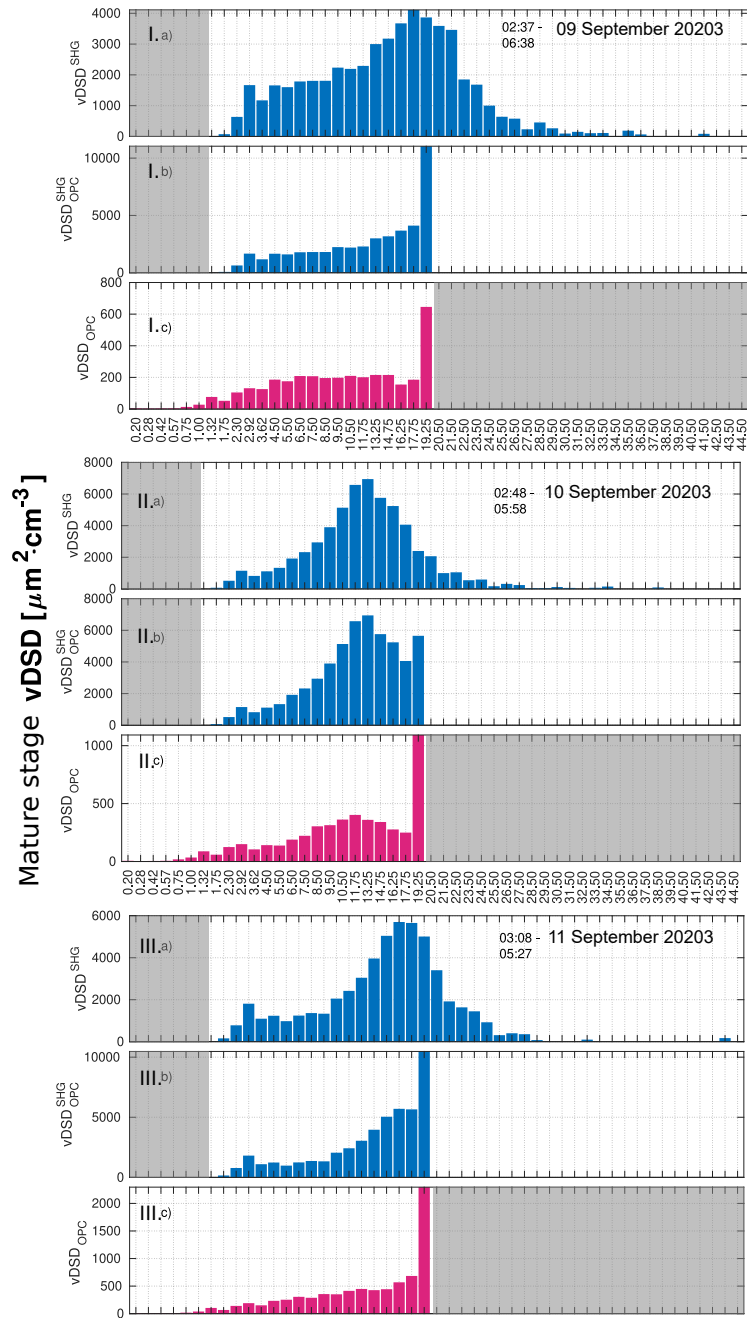


Figure 10. vDSD near ground for mature stage of night events of fog on: I. 08-09 Sep., II. 09 - 10 Sep., III. 10-11 Sep. 2023. Panels a) and b) presents the vDSD obtained from Shadowgraph, while c) presents vDSD from OPC-N3. The x axis represents the edges of the bins of droplet radii measured by OPC-N3, plus additionally greater bins (above 20 μm) visible only by Shadowgraph. The panels b) presents the same vDSD as panel a) however all the droplets with radius greater than 20 μm are counted as part of the last bin of OPC-N3 (18.5-20 μm) - this is done to be able to compare the vDSD from OPC-N3 and Shadowgraph. The imaging area for a given device is marked in white.

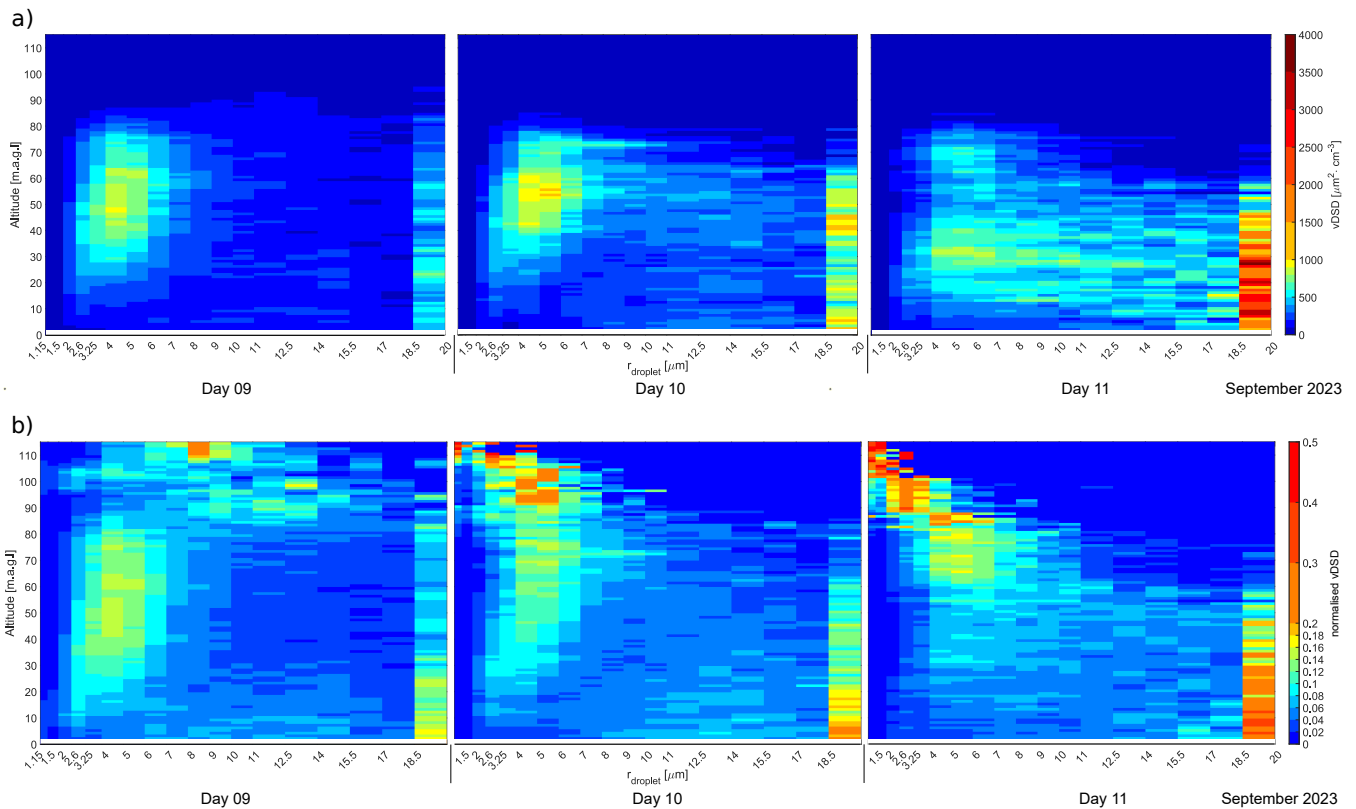


Figure 11. Vertical profile of vDSD and normalized vDSD for 8-11 September 9-11 Sep. 2023 fog occurrence. Panel a) presents the vDSD. The scale is divided into steps of $100 \mu\text{m}^2 \cdot \text{cm}^{-3}$ from 0 to $1000 \mu\text{m}^2 \cdot \text{cm}^{-3}$ and then in steps of $500 \mu\text{m}^2 \cdot \text{cm}^{-3}$. Panel b) presents the normalized at each height vDSD. Figure The figure presents what percentage of the entire spectrum at a given height is contributed by the volume of drops from a given bin.

675 Figure 11a) with vDSD presents on which height is produced most LWC indicates the altitudes where most LWC is produced and by which droplets, meanwhile droplet sizes, while Fig. 11-b) allows to analyze the spectrum in region where LWC is low (e.g. at top of fog layer, while vanishing) enables analysis of the droplet spectrum in regions with low LWC — such as near the top of the fog layer or during dissipation. Apart from vDSD for the whole episode, in the Appendix are shown vDSD (Fig. A6) for each stage of fog: beginning, mature, disappearing. In this section is describe and disappearing. This section describes how
 680 LWC, LWP and, and the droplet spectrum evolve during the occurrence of fog fog occurrence for each night case.

From vDSD (Fig. 11) it is visible that most of the LWC is associated with two drop radius regions. First The first region is described by an asymmetric distribution. The maximum value of the distribution is associated with a radius 4-5 μm . The distribution has a bigger slope from on the left side (droplets smaller than the maximum). Second The second region is a peak for droplets of radius bigger than $18.5 \mu\text{m}$ ($r_{>18.5}$). Big droplets are found in the whole range of altitudes, however there is;
 685 however, there are more of them when closer to the ground. In-

In the 10 m region-layer closest to the ground droplets with $r > 18.5$ are contributing to total LWC, droplets with $r > 18.5 \mu\text{m}$ contribute up to 40% of the total LWC. Within this layer, also when the closer to the ground surface, the smaller the contribution to LWC is made by droplets below $7 \mu\text{m}$ and larger by those above $7 \mu\text{m}$ from droplets with $r < 7 \mu\text{m}$, and the larger the contribution from droplets with $r > 7 \mu\text{m}$.

690 Above 10 m, the situation is reversed: droplets with $r < 7 \mu\text{m}$ contribute more to LWC than those with $7 \mu\text{m} < r < 18.5 \mu\text{m}$. Above 40 m with increasing height, with increasing altitude, the 4-5 μm peak shifts towards larger droplets of the order of 8-9 μm peak in the normalized vDSD gradually shifts toward larger droplet sizes, reaching approximately 8-9 μm .

Near the ground was located ShadowGraph, Figure 10 presents the comparison between the vDSD obtained from ShadowGraph and OPC-N3. ShadowGraph shows that near ground there are droplets of radius greater than $20 \mu\text{m}$, and that in case of OPC-N3 those droplets are counted in the last bin. Although OPC-N3 is not calibrated to match the vDSD values it has similar pattern of the spectrum as ShadowGraph.

695 vDSD near ground for mature stage of night events of fog on: I. 08-09 Sep., II. 09-10 Sep., III. 10-11 Sep. 2023. Panels a) and b) presents the vDSD obtained from Shadowgraph, while c) presents vDSD from OPC-N3. The X axis is representing the radius bins same as in OPC-N3 plus additionally greater bins (above $20 \mu\text{m}$) visible only by Shadowgraph. The panels b) presents the same vDSD as panel a) however all the droplets with radius greater than $20 \mu\text{m}$ are counted as part of the last bin of OPC-N3 ($18.5-20 \mu\text{m}$) - this is done to be able to compare the vDSD from OPC-N3 and Shadowgraph. The imaging area for a given device is marked in white. The maximum CTH during fog on 9 September was approximately 102 m. In most cases, the LWC above 80 m was below $0.2 \text{ g}\cdot\text{m}^{-3}$, indicating only sparse droplets in this region. Just above the CTH, most of the water was accumulated in droplets with radii between 8 and $14 \mu\text{m}$. With increasing height, this droplet size range decreased.

700 Subsequent fogs fog nights had increasingly larger LWC, this at a specific height (see Fig. 6). Even though LWC was reaching higher values on 10 September than on 9 September. The LWP was higher on 9 September because the fog was reaching higher altitudes. The increase of LWC was related to the appearance of droplets in the size of 7-17 μm , and not to the increase in the number of droplets in the size of 4-5 μm . The fog on night 08-09 Sep. had maximum CTH at 102 m, the LWC above 80 m was below $0.2 \text{ g}\cdot\text{m}^{-3}$. To LWC mostly contributed droplets of radius 8-14 μm . Above CTH the most water is in the form of small droplets with has decreasing radius with increasing altitude.

705 In the Appendix the Fig. A6 presents vDSD for three stages of fog for each day. Even in the initial stage of the fog, there were already large drops with $r > 18.5$, and the fog started to grow in thickness from the bottom. In the case of the fog from the nights of 8-9 and 9-10 Sep. 9 and 10 September, with increasing height, water was stored by drops with increasingly larger radii between 2-10 μm . In the case of the fog from the night of 10 to 11 Sep. September, with increasing height, an inverse relationship occurs - increasingly smaller drops store the most water from the range of radii 2.0-18.5 μm .

715 In the case of 08-09 and 10-11 Sep., dissipating stage of fog on 09 and 11 September, the CTH did not decrease; it remained around 80 m. While below 30 m, the vDSD shows minimal signal (bottom panels of Fig. A6), suggesting a very low droplet concentration in this region. This suggests that the fog disappeared more from the bottom than from the top. For the case of 9-10 Sep., only small drops from

720 As the profile of the dissipating fog on 10 September was taken approximately half an hour after the dissipation began, it captured only small droplets in the range of 2-7-7 μm at a height of 20-60 m contributed to the LWC. For heights between 20 and 60 m. In all cases, large drops droplets ($r_{>18.5}$ stopped contributing-) ceased to contribute significantly to the LWC when the fog was disappearing during the fog dissipation phase.

4.4 Optical, microphysical and radiation closure

725 ~~The optical, microphysical and radiation closure was done for the case study in the valley of Strzyżów city in September 2023.~~ A radiative closure was performed to assess the consistency between observed radiative fluxes and the microphysical measurements. Given that the OPC-N3 is a low-cost optical particle counter, we wanted to verify whether the vertical profiles of microphysical parameters were representative of actual conditions. Since no independent method was available, we used the obtained microphysical parameters as input for radiative transfer simulations. These simulations enabled us to test whether the
730 microphysical measurements from the OPC-N3 are consistent with the observed radiative fluxes.

Radiative transfer simulations were conducted using the Fu-Liou model in 1D mode, incorporating detailed vertical profiles of thermodynamic and microphysical properties. The model covers six shortwave and twelve longwave spectral bands, with input data including fog microphysics, aerosol optical properties, and surface reflectance. The fog droplet asymmetry parameter was calculated using Mie theory, based on measurements of liquid water content and droplet size. Details of the model setup
735 are provided in Section 3.4.

For performing the simulations, only cases when setup 1 (with OPC-N3) was attached to the balloon and data were properly collected. ~~In total there were 41 soundings.~~

On the Figure 13 and 14 by black line are presented the measured SW and LW radiation fluxes from were used. The simulated shortwave (SW) and longwave (LW) fluxes were compared with fluxes registered at the SolarAOT^{upper} and SolarAOT_{lower}
740 station. By the yellow dashed line is presented the simulation result for clear sky, while the orange circles present the result of simulation with implemented fog conditions, based on soundings. During 09 Sep. there were observed cirrus clouds therefore the SW radiation during the day at SolarAOT station has a rugged time course. During the day 10 Sep. stations. Two flights on 11 September between 05:40 and 06:22 were excluded from the radiative closure analysis due to suspected water condensation on the lower LW radiometer during fog dissipation. In total, there were 37 soundings used for analysis.

745 Fig. 12 compares SW and LW radiation between the model and observations at the sky was clear but during dust long-range transport. To compare the SolarAOT^{upper} and SolarAOT_{lower} stations. The scatter plots also show linear fits to the data. The left panels present the model results for clear-sky conditions between model and observation data from 10. Sep. was used. The comparison is show in the Fig. 12, as well as the comparison between fog modeled cases and observational data. Model was run with the use of meteorological soundings from based on observations from 10 September, while the right panels present
750 results from the time when there were fog conditions during days 9-11 September.

Upper-air temperature and humidity profiles were taken from balloon soundings by the Polish Meteorological and Water Management Institute in Tarnów station — which are done only twice per day, available only twice daily (00 and 12 UTC. Therefore UTC), resulting in limited temporal resolution above 100 m. In contrast, near-surface profiles were measured more

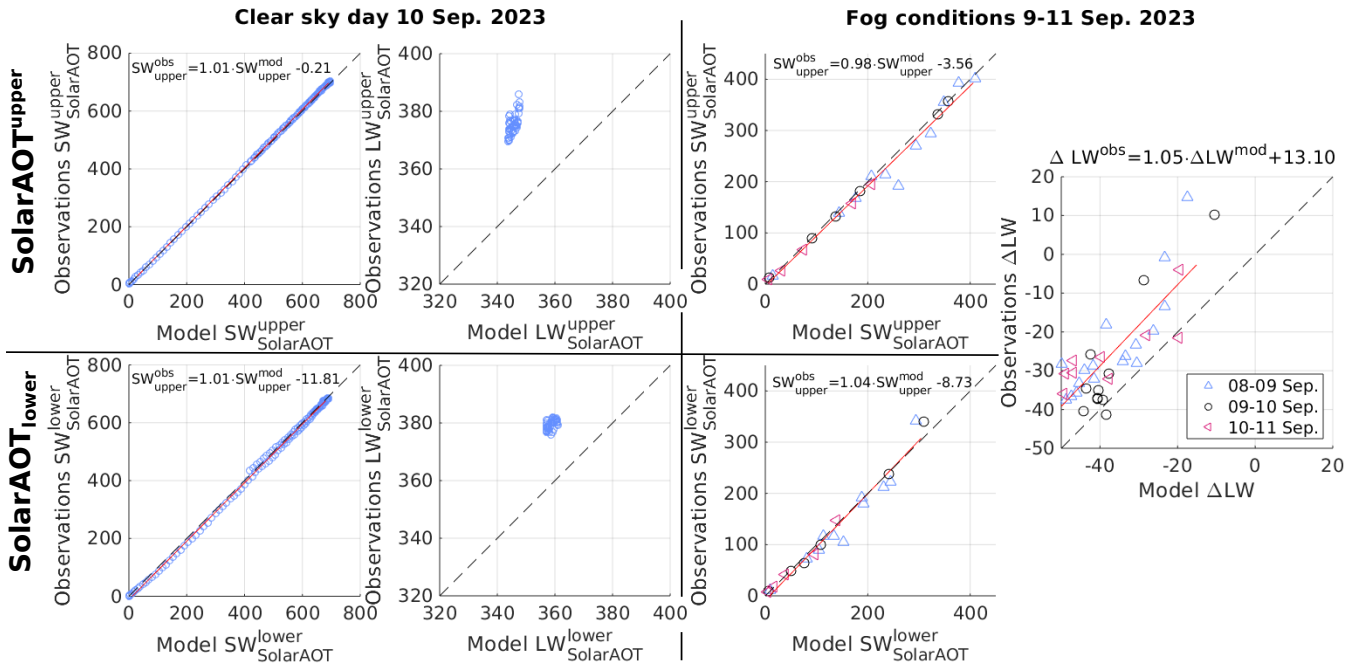


Figure 12. Scatter plots comparing observed and modeled SW (first and third column from left) and LW fluxes under clear-sky (left two columns) and fog conditions (right two columns). The last column presents the difference (Δ) between upper and lower station measurements for observed and modeled LW flux in fog conditions. The red solid line indicates the linear fit to the data. Blue triangles represent measurements from the night of 8–9 Sep., black circles show fog data from the night of 9–10 Sep., and pink triangles correspond to data collected during the night of 10–11 Sep. 2023. The equation for each fit is shown in the corresponding panel.

frequently on site (when fog was present). Therefore, for comparison of clear-sky conditions in model and observation, only data from near the sounding at 12 UTC \pm 2 hours were used.

On the scatter plots are shown also linear fits to the data. The SW radiation for-

The equation describing the relationship between the SW radiation under clear-sky and fog conditions for both stations is has a relation of almost 1:1 from the observation and model:-

$$SW_{upper}^{obs} = 1.01 \cdot SW_{upper}^{mod} - 0.3$$

$$SW_{lower}^{obs} = 1.01 \cdot SW_{lower}^{mod} - 11.7$$

Similarly in the case of model with implemented fog (note that upper site was above the fog layer):-

$$SW_{upper}^{obs} = 1.00 \cdot SW_{upper}^{mod} - 6.1$$

$$SW_{lower}^{obs} = 1.05 \cdot SW_{lower}^{mod} - 9.7$$

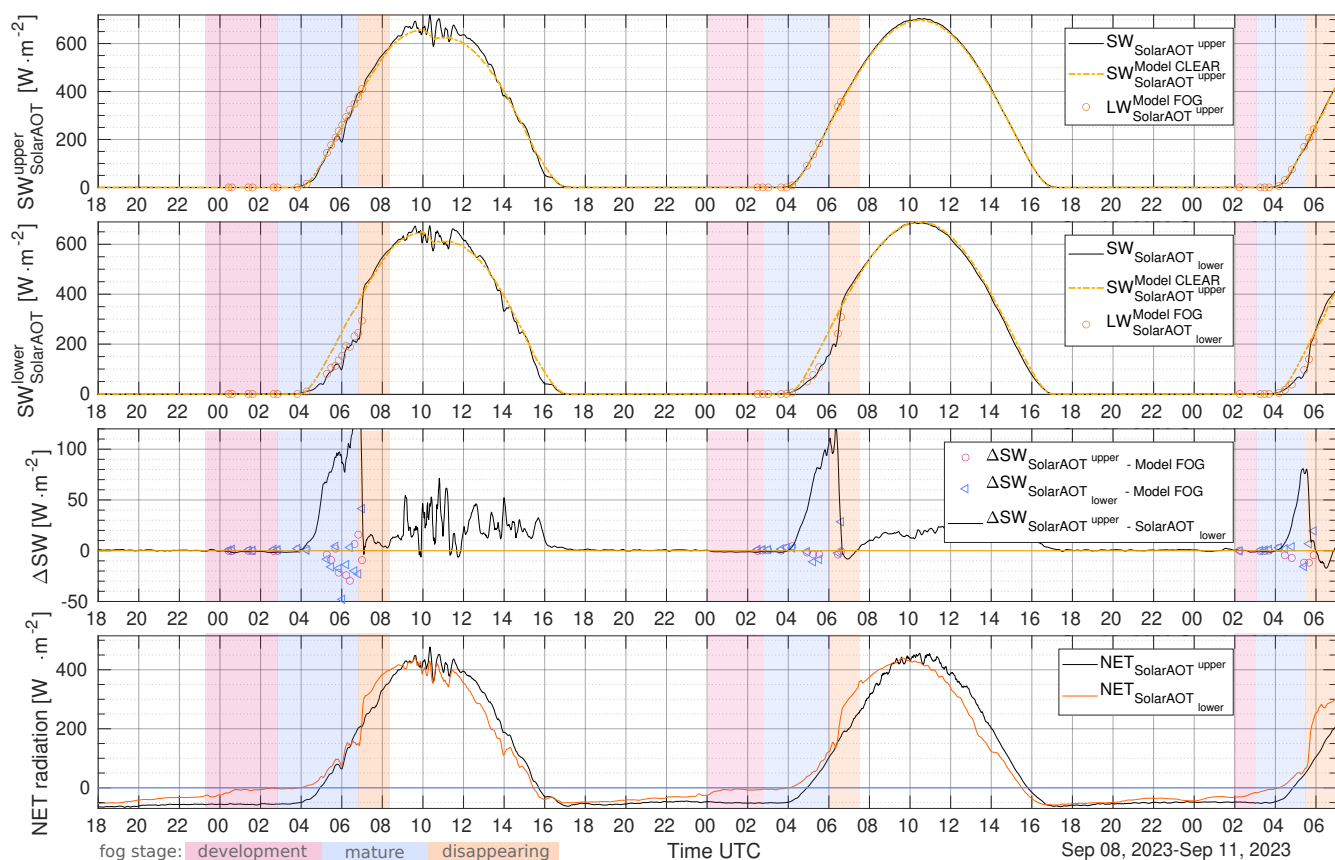


Figure 13. Comparison of observational data with model predictions of Incoming SW (Panel a, c, e, g) and LW (Panel b, d, f, h) fluxes for two locations: SolarAOT^{upper} (Panels a-d) and SolarAOT_{lower} station (Panels e-f)). Panels a, b, c) The black solid line measured data, f) presents the situation with clear-sky yellow dashed line - model results for no fog conditions which were on Sep. 10. Panels e, d, g, h) presents the comparison of SW and LW radiation during orange circles - model results for fog conditions measured by soundings. Red solid line presents The third panel from the linear fit to top presents the data, blue triangles data from night difference in SW flux between 8 and 9-September lower site (solid line), black pink circles fog data from night represent the difference between 9 and 10-September SolarAOT^{upper} station and pink model when fog conditions were implemented. Blue triangles represents data taken during night from 10 to 11-September 2023. represent the difference between the SolarAOT_{lower} station and the model with implemented fog conditions. The equation for each fit is presented above corresponding lowest panel presents the total net radiation for SolarAOT^{upper} (black line) and SolarAOT_{lower} station (orange line).

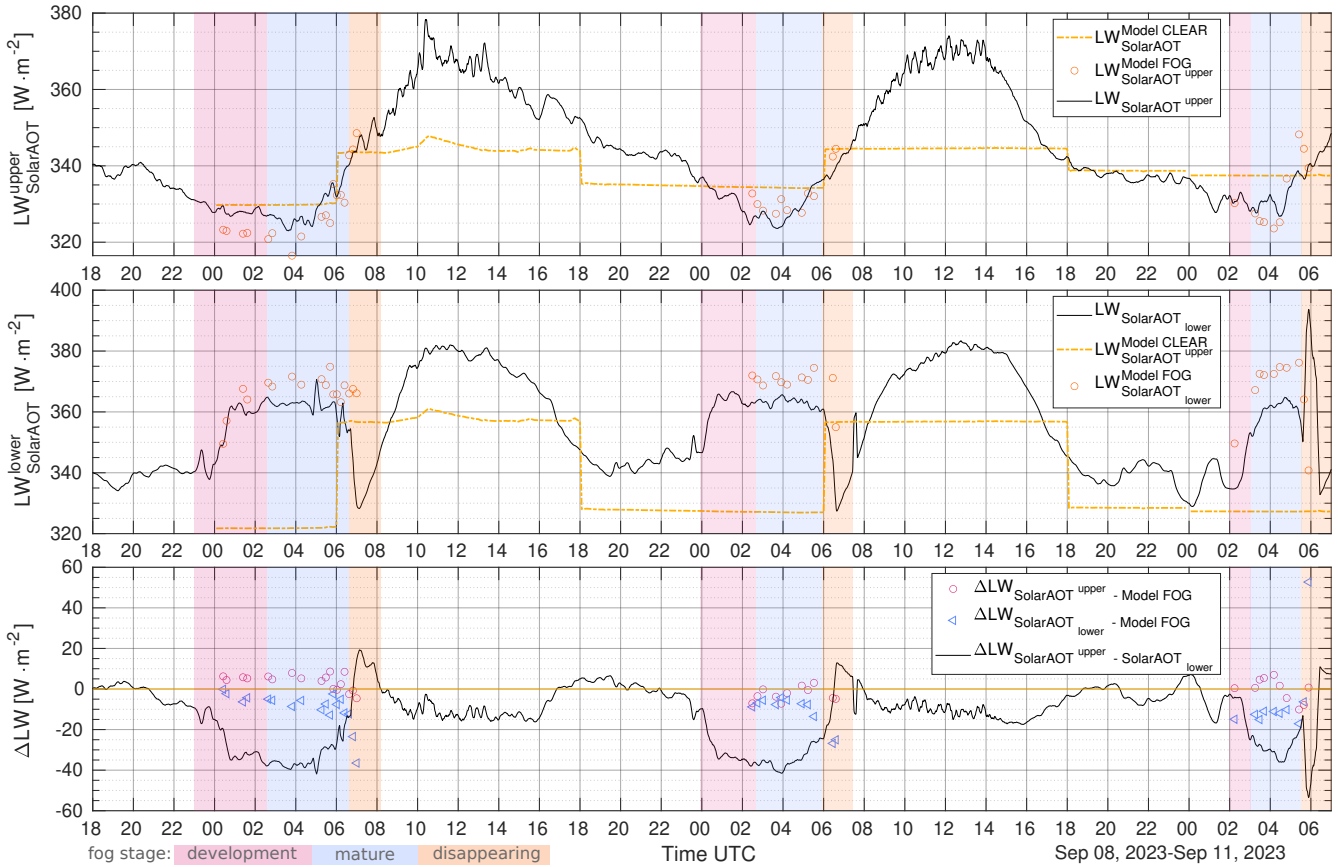


Figure 14. Incoming LW flux for SolarAOT^{upper} (upper panel) and SolarAOT_{lower} station (middle panel). The black solid line measured data, the yellow dashed line - model result for no fog conditions, the orange circles - model results for fog conditions measured by soundings. Lower panel presents with solid line difference in LW flux between SolarAOT^{upper} and SolarAOT_{lower} station, pink circles represent difference between upper station and model with fog conditions implemented and blue triangles represent difference between lower station and model with fog conditions.

The obtained linear fit is worse in the case of LW radiation for fog conditions¹. The offset is up to $-12 \text{ W}\cdot\text{m}^{-2}$. As fog is occurring mostly at night there is smaller variability of

770 Given the limited variation in LW downward radiation and the uncertainties introduced by sparse temperature soundings, absolute comparisons via regression provide limited insight. Instead of separate scatter plots for two stations, we present the difference in LW radiation between the upper and lower stations. The offset of the linear fit by $13.10 \text{ W}\cdot\text{m}^{-2}$ suggests that the fog implemented in the model can be too thick.

775 Figures 13 and 14 show the temporal comparison of SW and LW fluxes between the model and observations at the SolarAOT^{upper} and SolarAOT_{lower} stations. Black lines show the measured incoming SW and incoming LW radiation fluxes. By the yellow dashed line is presented the simulation result for clear-sky, while the orange circles present the result of the simulation with implemented fog conditions, based on soundings. The difference between observations and the model is shown in Fig. 14 on the lower panel for LW flux and mostly points are located in one area. One data point stands out from the rest, for 10-11 Sep., this is at the dissipation of fog, when the sounding did not show fog and the instruments showed the opposite.

$$LW_{upper}^{obs} = 0.53 \cdot LW_{upper}^{mod} + 164.5$$

780 $LW_{lower}^{obs} = 0.38 \cdot LW_{lower}^{mod} + 217.4$

The in Fig. 13 on the second panel from bottom for SW flux. Additionally, the Table 2 presents the statistics between simulated and measured SW and LW flux for clear-sky (no fog) and fog conditions.

785 For clear-sky SW radiation, the model flux at the SolarAOT^{upper} station are underestimated, RMSE (is underestimated. The root mean square error (RMSE) for 9 and 10 Sep. is accordingly 25.5 and 5.4 $\text{W}\cdot\text{m}^{-2}$. Relatively high RMSE during, respectively. On 9 Sep. is due September, the SW radiation at the SolarAOT^{upper} station exhibits a rugged temporal pattern due to the presence of cirrus clouds. The relatively high RMSE on this day is attributed to cirrus cloud contamination, which was not considered accounted for in the radiative transfer model. For the SolarAOT_{lower} station, the RMSE is 22.9 and 10.4 23.1 and 10.5 $\text{W}\cdot\text{m}^{-2}$, respectively, for 9 and 10 Sep. September.

790 The model LW flux at both sites is underestimated and RMSE does not exceed 26 for clear-sky conditions is underestimated, and the RMSE exceeds 30 $\text{W}\cdot\text{m}^{-2}$. The model shows slightly better agreement during fog conditions for the upper station. Running the model based solely on aerological soundings performed twice daily does not allow for an accurate representation of the diurnal variation of LW radiation. The results show significant discrepancies between the model and observations at both the upper and lower stations. To better reproduce the temporal evolution of IR radiation, more detailed information on the distribution of RH in the lower atmospheric layer is required.

795 When the fog conditions were applied the results for The results indicate that when fog conditions are included, the model reproduces both SW and LW fluxes reasonably well at both stations. This is due to inputting more information from our soundings. For the SolarAOT^{upper} station where, SW fluxes are slightly overestimated (up to $12.7 \text{ W}\cdot\text{m}^{-2}$) for SW flux and underestimated (up to -10 , while LW fluxes show deviations within $\pm 4 \text{ W}\cdot\text{m}^{-2}$) for LW flux. In the case of the SolarAOT_{lower},

MBE [$\text{W}\cdot\text{m}^{-2}$]						
Night between	08-09 Sep.		09-10 Sep.		10-11 Sep.	
Model run	every 5 min	when sounding	every 5 min	when sounding	every 5 min	when sounding
Fog implementation	no	yes	no	yes	no	yes
Time	7-17 UTC	4-7 UTC	7-17 UTC	4-7 UTC	7-17 UTC	4-7 UTC
$I_{\text{SolarAOT}^{\text{upper}}}$	-12.9 ± 22.3	12.7 ± 23.1	-4.5 ± 2.9	1.4 ± 3.3	-	6.5 ± 5.8
$I_{\text{SolarAOT}^{\text{lower}}}$	-1.0 ± 23.1	8.2 ± 23.7	6.7 ± 8.1	-1.5 ± 15.4	-	-0.3 ± 8.9
$I_{\text{SolarAOT}^{\text{lower}}} (-\text{cirrus bias})$	11.9 ± 13.9	0.8 ± 26.0				
Time	10-14 UTC	0-7 UTC	10-14 UTC	0-7 UTC		0-7 UTC
$IR_{\text{SolarAOT}^{\text{upper}}}$	-29.9 ± 2.9	-3.7 ± 3.8	-32.4 ± 2.3	2.6 ± 3.4	-	0.3 ± 6.0
$IR_{\text{SolarAOT}^{\text{lower}}}$	-20.7 ± 1.5	9.3 ± 8.6	-22.3 ± 3.1	10.8 ± 7.9	-	12.2 ± 3.3

RMSE [$\text{W}\cdot\text{m}^{-2}$]						
Night between	08-09 Sep.		09-10 Sep.		10-11 Sep.	
Model run	every 5 min	when sounding	every 5 min	when sounding	every 5 min	when sounding
Fog implementation	no	yes	no	yes	no	yes
Time	7-17 UTC	4-7 UTC	7-17 UTC	4-7 UTC	7-17 UTC	4-7 UTC
$I_{\text{SolarAOT}^{\text{upper}}}$	25.7	25.4	5.4	3.3	-	8.4
$I_{\text{SolarAOT}^{\text{lower}}}$	23.1	24.0	10.5	14.1	-	8.0
$I_{\text{SolarAOT}^{\text{lower}}} (-\text{cirrus bias})$	18.2	24.8				
Time	10-14 UTC	0-7 UTC	10-14 UTC	0-7 UTC		0-7 UTC
$IR_{\text{SolarAOT}^{\text{upper}}}$	30.1	5.3	32.5	4.1	-	5.7
$IR_{\text{SolarAOT}^{\text{lower}}}$	20.8	12.5	22.5	13.2	-	12.6

Table 2. Statistics of SW (I) and LW (IR) flux comparisons between the model and observations at both sites. The mean bias error (MBE) and root mean square error (RMSE) were calculated for each day under fog and non-fog conditions. Additionally, for Sep. 9, the mean MBE and RMSE for the SW radiation were computed after removing the estimated cirrus-induced bias.

800 At the $\text{SolarAOT}^{\text{lower}}$ station, biases for both SW and LW ~~bias also do not exceed 10~~ fluxes remain within $12.2 \text{ W}\cdot\text{m}^{-2}$.
The RMSE ~~exceeds 20~~ generally stays below $14.2 \text{ W}\cdot\text{m}^{-2}$ ~~only during cirrus~~, except under cirrus cloud conditions (9 Sep.).
A slightly higher RMSE (SW and LW range) was obtained for the lower than for the upper station. Generally, an agreement
between SW and LW fluxes at both sites is really good. Even for fog conditions at the lower site the MBE is very low (up to 10
 $\text{W}\cdot\text{m}^{-2}$) and RMSE ~~not exceed 20~~ $\text{W}\cdot\text{m}^{-2}$ (September). The RMSE values for LW radiation at the lower station are approximately
805 $12\text{--}13.5 \text{ W}\cdot\text{m}^{-2}$ during fog conditions, indicating that the chosen fog microphysical parameters — liquid water content LWP
and τ_{eff} — adequately represent the fog's thermal radiative properties. The relatively low deviation suggests that the modeled
fog layer produces realistic LW fluxes near the surface, supporting the suitability of the microphysical assumptions for the
observed conditions. Due to model simplifications, the fog is assumed to have a constant droplet size and LWC at all heights,
which may introduce some uncertainty into the results. As can be seen from the temporal comparison of LW radiation from

810 model and data (Fig. 14) most of the model overestimation occurs during the fog decay stage; these errors may result from the lack of homogeneity, the patchwork nature of the fog during its decay. Overall, these results demonstrate that the model captures the radiative fluxes with acceptable accuracy during fog events.

4.5 Radiative Fluxes During Fog Events

The apparatus at SolarAOT~~upper and lower~~^{upper} and SolarAOT~~lower~~^{lower} station measures the total net radiation (NET; downward
815 ~~by~~ minus upward SW+LW fluxes), which is presented on the lowest panel of Fig. 13. During the first night of observations, it is visible that between 00:00 and 00:~~40-44~~ the NET radiation at the SolarAOT~~lower~~^{lower} station changed from ~~-20-24.4~~ to $-6 \text{ W}\cdot\text{m}^{-2}$. After the development of fog, the NET radiation at the lower station was around $0 \text{ W}\cdot\text{m}^{-2}$ ~~it become positive after the~~. It became positive after sunrise. The difference between lower and upper station NET radiation during night fog was around ~~60-50~~ $\text{W}\cdot\text{m}^{-2}$. When the fog disappeared (7:00)~~there is~~, there was a visible abrupt jump of ~~160-156~~ $\text{W}\cdot\text{m}^{-2}$ at
820 the lower station within 15 minutes. For the night 9-10 ~~Sept~~-September 2023, the fog also started to develop around midnight (at 00:50 the NET radiation was ~~-6-5.8~~ $\text{W}\cdot\text{m}^{-2}$). ~~The~~ NET radiation at SolarAOT~~lower~~^{lower} ~~become~~^{became} positive after sunrise, and a jump of ~~140-134~~ $\text{W}\cdot\text{m}^{-2}$ occurred at the moment of ~~disappearing of fog~~ disappearance at 6:20-6:~~35-40~~.

During the last night of observations, the NET radiation at the lower station was ~~still-30-44~~ $\text{W}\cdot\text{m}^{-2}$ at 02:00. ~~From midnight while at upper station -49~~ $\text{W}\cdot\text{m}^{-2}$. Starting at 02:00 ~~the NET radiation was constantly increasing until the sunrise when~~, the net
825 radiation gradually increased from approximately $-30 \text{ W}\cdot\text{m}^{-2}$ and reached $0 \text{ W}\cdot\text{m}^{-2}$ at sunrise. The fog disappeared quickly, in less than ten minutes, at 05:35 the NET radiation changed by ~~120-125~~ $\text{W}\cdot\text{m}^{-2}$. ~~SW flux for SolarAOT upper and lower station. Black solid line measured data, yellow dashed line—model result for no fog conditions, orange circles—model results for fog conditions measured by soundings. Third panel from the top presents difference in SW flux between upper and lower site (solid line), pink circles represents difference between SolarAOT upper station and model when there were implemented fog conditions. Blue squares represent difference between SolarAOT lower station and model with implemented fog conditions. The lowest panel presents the total net radiation for SolarAOT upper (black line) and SolarAOT lower station (orange line). LW flux for a) upper and b) lower station. Black solid line measured data, yellow dashed line—model result for no fog conditions, orange circles—model results for fog conditions measured by soundings. Panel c) presents with solid line difference in LW flux between SolarAOT^{upper} and SolarAOT_{lower} station, pink circles represent difference between upper station and model with fog conditions implemented and blue squares represent difference between lower station and model with fog conditions.~~

835 ~~Day Model run every 5 min when sounding every 5 min when sounding every 5 min when sounding~~ **Fog implementation no yes no yes no yes** Time 7-17 UTC 4-7 UTC 7-17 UTC 4-7 UTC 7-17 UTC 4-7 UTC $I_{\text{SolarAOT}^{\text{upper}}}$ -12.6 ± 22.3 10.2 ± 23.8 -4.5 ± 2.9 1.7 ± 3.3 -4.9 ± 5.8 $I_{\text{SolarAOT}^{\text{lower}}}$ -0.8 ± 23.0 6.1 ± 22.8 6.7 ± 8.1 -1.2 ± 14.6 -4.6 ± 10.4 $I_{\text{SolarAOT}^{\text{lower}}} (-\text{cirrus bias})$ 11.8 ± 13.7 1.0 ± 23.3 Time 10-14 UTC 0-7 UTC 10-14 UTC 0-7 UTC 0-7 UTC $IR_{\text{SolarAOT}^{\text{upper}}}$ -22.4 ± 4.4 -10.2 ± 6.4 -25.1 ± 4.2 -5.0 ± 3.4 -7.6 ± 5.4 $IR_{\text{SolarAOT}^{\text{lower}}}$ -20.7 ± 1.5 8.6 ± 8.8 -22.3 ± 3.1 10.2 ± 7.8 -4.0 ± 20.5 Day Model run every 5 min when sounding every 5 min when sounding every 5 min when sounding **Fog implementation no yes no yes no yes** Time 7-17 UTC 4-7 UTC 7-17 UTC 4-7 UTC 7-17 UTC 4-7 UTC $I_{\text{SolarAOT}^{\text{upper}}}$ 25.5 24.9 5.4 3.4 -7.3 $I_{\text{SolarAOT}^{\text{lower}}}$ 22.9 22.7 10.4 13.3 -10.7 $I_{\text{SolarAOT}^{\text{lower}}} (-\text{cirrus bias})$ 18.0 22.4 Time 10-14 UTC 0-7 UTC 10-14 UTC 0-7 UTC 0-7 UTC $IR_{\text{SolarAOT}^{\text{upper}}}$ -22.8

12.0-25.4-6.0-9.2 IR_{SolarAOT^{lower}}-20.8-12.1-22.5-12.6-19.9 Statistics of SW (I) and LW (IR) flux comparison between model
845 and observation at both sites. The MBE (mean bias error between model and observation) and RMSE were calculated for each
day and for fog and non-fog conditions. In addition, for September 9 the mean MBE and RMSE for the SW radiation was
calculated with removed estimated cirrus bias.

Having information on radiation fluxes at two levels allows ~~to investigate~~ for investigating the sensitivity of the change in
LW radiation by the fog LWP. Fig. 15 shows the relationship between the modeled LWP content and the modeled difference in
850 LW radiation between the upper and lower ~~station~~ stations. In addition to the modeled values, the lower panel of Fig. 15 shows
the relationship for the data observed at both stations and the measured LWP on the balloon ~~LWP~~ in the fog. In both graphs,
the data ~~are arranged according to~~ exhibit a linear relationship (Pearson correlation coefficient for modeled data is ~~-0.81~~ and for
~~observation is -0.59~~), with Pearson correlation coefficients and corresponding p-values of -0.82 and 1.79e-10 for the model,
and -0.37 and 0.02 for the observations, respectively. A straight line was fitted to the modeled data ~~was fitted a straight line~~
855 ~~given by equation:~~, given by the equation:

$$\Delta \text{IR} = \underline{-1.47-1.09} [\text{W g}^{-1}] \cdot \text{LWP} \underline{-4.16-13.42} [\text{W m}^{-2}] \quad (17)$$

~~to~~ To the observed data was fitted a straight line:

$$\Delta \text{IR} = \underline{-1.17-0.74} [\text{W g}^{-1}] \cdot \text{LWP} \underline{-5.87+12.25} [\text{W m}^{-2}]. \quad (18)$$

860 5 Conclusions

The purpose of this study was to capture vertical profiles of the microphysical and thermodynamic characteristics within
fog layers, ~~utilizing~~ using in situ data ~~gathered~~ collected by a tethered balloon during ~~the a~~ field campaign. ~~In this article~~
~~are analyzed~~ This article analyzes three cases of radiative fog ~~which occurred in~~ that occurred in the valley of Strzyżów
city (Southeastern Poland) in September 2023. In total ~~there were performed,~~ 74 soundings ~~, of which 41 were done with~~
865 ~~were performed,~~ 41 of which included measurements with the OPC-N3 ~~which allows for droplet spectra calculations.~~ The
~~observed three cases had similar weather conditions (temperature - T_{sensor}, enabling the calculation of droplet size spectra. The~~
~~three observed cases exhibited similar meteorological conditions, including temperature (T), relative humidity -RH, (RH), and~~
~~aerosol scattering coefficient at 525nm (ASC₅₂₅).~~ For each case, the liquid water path (LWP) exceeded 15 g·m⁻², ~~none of the~~
~~eases transitioned to~~ and in most instances, the fog did not transition into thick fog.

870 ~~In case of the~~ the case of quasi-adiabatic ~~boundary clouds Brenguier et al. (2000)~~ boundary-layer clouds Brenguier et al. (2000)
, the droplet number concentration (N_c) ~~was~~ remains constant with height, and the increase ~~of in~~ liquid water content (LWC)
with height ~~was~~ is primarily associated with the ~~increase~~ growth of droplet radii. ~~In~~ Similarly, simulations of Atlantic stratocu-
mulus ~~used by Chang and Li (2002) also increase of~~ conducted by Chang and Li (2002) showed that the increase in LWC with
height was ~~associated with the increase~~ droplet radii. ~~However in this study, were we examine~~ also linked to an increase in
875 droplet size.

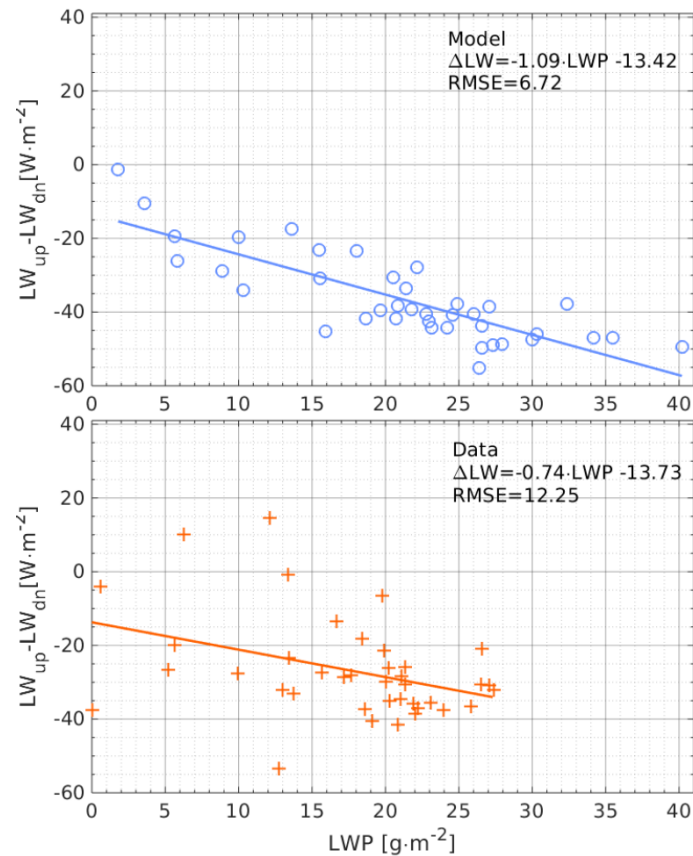


Figure 15. Relation between fog LWP (for days 8-11 September-9-11 Sep. 2023) and the difference of LW downwards flux between the upper and lower SolarAOT stations. The upper panel presents the radiation transfer model simulations and the lower panel corresponds to the balloon profiles (LWP) and te-radiometer observation-observations at the upper and lower SolarAOT stationstations.

880 However, in the present study, which focuses on fog conditions, the observed changes-of-LWC-were-mostly-associated-with the variation of variations in LWC were primarily associated with changes in N_c . This means that the change of LWC is mostly associated with indicates that the increase in LWC is mainly due to the activation of fog droplets on the new nuclei than with growth by collision-coalescence new condensation nuclei, rather than droplet growth through the collision-coalescence process. Similar results were obtained-reported by Okita (1962); Egli et al. (2015), which-also-studied-who also investigated the vertical distribution of microphysical properties in radiation fogs. In-

885 In the three presented cases of radiation fog over the Strzyżów valley we-obtained-, we observed that the effective radius (r_{eff}) is-dropping-eff) decreases with height. This is in-line-consistent with Okita (1962) and partially with the observations of Egli et al. (2015) (in his study r_{eff} was dropping with height for some observations but mostly was-, reff decreased with height in some cases, but was mostly constant with height). With-the-development-of-fog-As the fog developed, the decrease of r_{eff} with height is-less-pronounce-but still-became less pronounced, but remained visible.

In the work of Okita (1962) ~~big, large~~ droplets are mostly concentrated near the ground (the volume radius of ~~big droplets decrease large droplets decreases~~ with height). In our study, drops larger than $18.5 \mu\text{m}$ appear in the spectrum. ~~DSD DSDs~~ with small concentrations of drops ~~grater greater~~ than $30 \mu\text{m}$ were observed in experiments conducted by ~~Wendish et al. (1998); Gultepe et al. (2009); Mazoyer et al. (2022)~~. ~~Those big~~ (Wendish et al., 1998; Gultepe et al., 2009; Mazoyer et al., 2022). ~~These large~~ droplets are the result of collision-coalescence and Ostwald ripening processes. ~~In presented study-~~

~~In the presented study,~~ the volume of water is contained in two ranges of droplet radii. ~~One is around 4-5; one around 4-5~~ μm and the other ~~is~~ above $18.5 \mu\text{m}$. Even though droplets ~~of radii grater with radii greater~~ than $18.5 \mu\text{m}$ are rare, the amount of water ~~carried by them they carry~~ is significant. The significance of the first range increases with height, while ~~that~~ of the second range decreases with height.

Simulations of numerical weather prediction (NWP) and large eddy simulations (LES) are predominantly based on bulk parametrization of e.g., LWP and N_c ~~Bergot et al. (2007); Khain et al. (2015)~~ (Bergot et al., 2007; Khain et al., 2015). For improved NWP and LES simulations of fog formation and dissipation, it is essential to incorporate the droplet spectrum across the fog layer ~~Thoma et al. (2011)~~ (Thoma et al., 2011). This would enable the removal of larger droplets through sedimentation, potentially alleviating the issue of excessively high LWC in fog forecasts ~~Philip et al. (2016); Pithani et al. (2019)~~ (Philip et al., 2016; Pithani et al., 2019).

In ~~analyzed three cases the fog is disappearing from the three analyzed cases, the fog dissipates from both the~~ top and bottom. In ~~mature stage the profile the mature stage, the profiles~~ of LWC and N_c ~~is growing increase~~ with height and then ~~after reaching maximum value decreasing to,~~ after reaching a maximum value, ~~decrease toward the~~ fog top height (CTH). During the ~~decreasing stage~~ ~~dissipation stage, the~~ region above the maximum N_c /LWC ~~is squeezed becomes compressed~~. The maximum N_c /LWC is located above 80% of ~~the~~ fog height.

At the bottom of the fog, the smallest droplets evaporate. As ~~there is no production of new droplets, the big droplets are falling down and are located mostly near to~~ no new droplets are formed, the larger droplets settle and are mostly located near the ground, which ~~reflects in is reflected in higher~~ r_{eff} ~~higher~~ r_{eff} values at the bottom of the fog. Droplets ~~of radius with radii~~ up to $40 \mu\text{m}$ can be described by an approximate formula for terminal velocity (u):

$$u(r) = k_1 \cdot r^2, \quad (19)$$

where ~~$k_1 \approx 1.19 \cdot 10^6$~~ $k_1 \approx 1.19 \cdot 10^6 \text{ cm}^{-1} \cdot \text{s}^{-1}$ ~~Yau and Rogers (1996)~~ (Yau and Rogers, 1996). Using this formula, the fall velocity for drops larger than $18.5 \mu\text{m}$ is 4.07 cm/s . In the absence of droplet growth and turbulence, for example ~~drops with radius, drops with a radius of~~ $18.5 \mu\text{m}$ will be removed within 7 minutes from a fog ~~of height layer~~ 100 m . ~~In the ease of soundings through m thick, During soundings conducted in~~ the final stage of the fog life cycle, no large drops are observed ~~because they have been washed away, as they have already settled out~~.

In the article, we calculated the theoretical equivalent adiabaticity (α_{eq}). The values of α_{eq} ~~were in ranged~~ between 0.0 - and 0.6, ~~similarly to previous values similar to values previously~~ reported for fog events. During one case ~~at the begging, at the early~~ stage of fog ~~the development, a~~ negative value of α_{eq} was observed (-3.2). ~~The elevated This~~ negative value was ~~caused by high LWC value at attributed to an elevated LWC near~~ the ground. In ~~literature events were LWC decrease the literature,~~

~~cases where LWC decreases~~ with height in fog ~~were are~~ rarely observed Costablos et al. (2024); Okita (1962); Boutle et al. (2018) ~~and as well~~, and are typically associated with thin fog layers, with CTH not exceeding 40 m.

For ~~studied cases the average fog-core LWC was between the studied cases, the average fog-core LWC ranged from 0.2 -0.4 to 0.4~~ $\text{g}\cdot\text{m}^{-3}$. LWC ~~was increasing from ground increased from the ground up~~ to approximately 60% ~~CTH height and then decreasing to CTH~~ of CTH, and then decreased toward the fog top. The mean N_c ~~was reached~~ up to 300 cm^{-3} . In two fog cases (Night 08-09 and 09-10 September) ~~nights of 8-9 and 9-10 September~~, the mean N_c with height could be approximated by a ~~parabola parabolic~~ curve. In the last fog case (10-11 September) ~~the N_c had 10-11 September~~, N_c exhibited two local maxima at 25% and 88% of CTH. The mean r_{eff} in all cases was around ~~8-10 8-10~~ μm and ~~was linearly decreasing decreased linearly~~ with height. ~~In~~

At the Strzyżów location ~~are mounted~~, solar and infrared radiometers ~~on are installed at~~ two different heights (~~in fog within the fog layer~~ and above it), ~~which allows for determining the impact of fog enabling assessment of the fog's impact~~ on radiation fluxes. ~~It A negative correlation~~ has been shown ~~that there is a negative correlation (for modeled data -0.81 and for observation -0.59)~~ between the difference in infrared radiation and the total water content in the fog ~~. The fog disappearing (Pearson correlation coefficients and corresponding p-values of -0.82 and 1.79e-10 for the model, and -0.37 and 0.02 for the observations, respectively).~~ The dissipation of fog can drastically change the total radiation ~~fluxes flux~~ at the ground within ~~a period of 10-30 min-10-30 minutes~~, by up to $160\text{ W}\cdot\text{m}^{-2}$.

During fog, the mean bias between observed and modeled radiation ~~flux is around fluxes is approximately~~ $2\text{ W}\cdot\text{m}^{-2}$ for ~~SW and 8 shortwave (SW) and 11 longwave (LW) radiation~~ at the lower station. The good agreement of radiative fluxes indicates the consistency of the measurement data on the physical properties of ~~the~~ fog.

Code and data availability. The data used in this article were uploaded to the repository. Nurowska, Katarzyna, 2024, "Microphysical and optical data of radiation fog in Strzyżów Valley, Poland", <https://danebadawcze.uw.edu.pl/privateurl.xhtml?token=30df09f8-ce75-4c28-83ee-53bdc1b1c4fc>, Dane Badawcze UW, V1.

Author contributions. K.N - Conceptualization, Methodology, Formal analysis, Investigation, Writing — original draft preparation, Writing—review and editing, Visualization; P.M. - lidar data visualisation; K.M. - Conceptualization, Supervision; All authors have read and agreed to the published version of the manuscript.

Competing interests. The authors declare no conflict of interest.

Acknowledgements. We thank the AERONET team, principal investigators and other participants for ~~theirs their~~ effort in establishing and maintaining the network. This research is part of the OPUS project (Polish Grant No. 2017/27/B/ST10/00549) *Impact of aerosol on the*

List of abbreviations:

Abbreviation	Description	Abbreviation	Description
AE	aerosol Angstrom Ångström exponent	MSE	mean bias error
α_{eq}	theoretical equivalent adiabaticity	MWR	microwave radiometer
AOD	aerosol optical depth	NTSB	American National Transportation Safety Board
ASC ₅₂₅	aerosol scattering coefficient of light at 525 nm	LES	large eddy simulations
CCN	cloud condensation nuclei	LW	longwave radiation
CTH	cloud / fog top height	LWC	liquid water content
DSD	droplet size distribution	LWC ₀	non-zero surface liquid water content
eBC	equivalent of black carbon	LWP	liquid water path
N _c	droplet number concentration	RH	relative humidity
NC	particle number concentration	RMSE	root mean square error
NWP	numerical weather prediction	SBL	stable boundary layer
p	pressure	SSA	aerosol single scattering albedo
PM	particle matter	SW	shortwave radiation
r _{eff}	effective radius	T	temperature
RH	relative humidity	vDSD	volume droplet size distribution

References

- Antoine, S., Honnert, R., Seity, Y., Vié, B., Burnet, F., and Martinet, P.: Evaluation of an Improved AROME Configuration for Fog Forecasts during the SOFOG3D Campaign, *Weather and Forecasting*, 38, 1605 – 1620, <https://doi.org/10.1175/WAF-D-22-0215.1>, 2023.
- 955 Bari, D., Bergot, T., and Tardif, R.: Fog Decision Support Systems: A Review of the Current Perspectives, *Atmosphere*, 14, <https://doi.org/10.3390/atmos14081314>, 2023.
- Bergot, T., Terradellas, E., Cuxart, J., Mira, A., Leichti, O., Mueller, M., and Nielsen, N. W.: Intercomparison of single-column numerical models for the prediction of radiation fog, *Journal of Applied Meteorology and Climatology*, 46, 504 – 521, <https://doi.org/10.1175/JAM2475.1>, cited by: 87; All Open Access, Bronze Open Access, 2007.
- 960 Bergot, T., Escobar, J., and Masson, V.: Effect of small-scale surface heterogeneities and buildings on radiation fog: Large-eddy simulation study at Paris–Charles de Gaulle airport, *Quarterly Journal of the Royal Meteorological Society*, 141, 285–298, <https://doi.org/https://doi.org/10.1002/qj.2358>, 2015.
- Betts, A. K.: Cloud Thermodynamic Models in Saturation Point Coordinates, *Journal of Atmospheric Sciences*, 39, 2182 – 2191, [https://doi.org/10.1175/1520-0469\(1982\)039<2182:CTMISP>2.0.CO;2](https://doi.org/10.1175/1520-0469(1982)039<2182:CTMISP>2.0.CO;2), 1982.
- 965 Boutle, I., Price, J., Kudzotsa, I., Kokkola, H., and Romakkaniemi, S.: Aerosol–fog interaction and the transition to well-mixed radiation fog, *Atmospheric Chemistry and Physics*, 18, 7827–7840, <https://doi.org/10.5194/acp-18-7827-2018>, 2018.
- Boutle, I., Angevine, W., Bao, J.-W., Bergot, T., Bhattacharya, R., Bott, A., Ducongé, L., Forbes, R., Goecke, T., Grell, E., Hill, A., Igel, A. L., Kudzotsa, I., Lac, C., Maronga, B., Romakkaniemi, S., Schmidli, J., Schwenkel, J., Steeneveld, G.-J., and Vié, B.: Demistify: a large-eddy simulation (LES) and single-column model (SCM) intercomparison of radiation fog, *Atmospheric Chemistry and Physics*, 22, 319–333, <https://doi.org/10.5194/acp-22-319-2022>, 2022.
- 970 Brenguier, J. L.: Parameterization of the Condensation Process: A Theoretical Approach, *Journal of Atmospheric Sciences*, 48, 264 – 282, [https://doi.org/10.1175/1520-0469\(1991\)048<0264:POTCPA>2.0.CO;2](https://doi.org/10.1175/1520-0469(1991)048<0264:POTCPA>2.0.CO;2), 1991.
- Brenguier, J.-L., Pawlowska, H., Schüller, L., Preusker, R., Fischer, J., and Fouquart, Y.: Radiative Properties of Boundary Layer Clouds: Droplet Effective Radius versus Number Concentration, *Journal of the Atmospheric Sciences*, 57, 803 – 821, [https://doi.org/10.1175/1520-0469\(2000\)057<0803:RPOBLC>2.0.CO;2](https://doi.org/10.1175/1520-0469(2000)057<0803:RPOBLC>2.0.CO;2), 2000.
- 975 Capobianco, G. and Lee, M. D.: The Role of Weather in General Aviation Accidents: An Analysis of Causes, Contributing Factors and ISSUES, *Proceedings of the Human Factors and Ergonomics Society Annual Meeting*, 45, 190–194, <https://doi.org/10.1177/154193120104500241>, 2001.
- Cermak, J. and Bendix, J.: Detecting ground fog from space – a microphysics-based approach, *International Journal of Remote Sensing*, 32, 3345–3371, <https://doi.org/10.1080/01431161003747505>, 2011.
- 980 Chang, F.-L. and Li, Z.: Estimating the vertical variation of cloud droplet effective radius using multispectral near-infrared satellite measurements, *Journal of Geophysical Research: Atmospheres*, 107, AAC 7–1–AAC 7–12, <https://doi.org/https://doi.org/10.1029/2001JD000766>, 2002.
- Costablos, T., Burnet, F., Lac, C., Martinet, P., Delanoë, J., Jorquera, S., and Fathalli, M.: Vertical Profiles of Liquid Water Content in fog layers during the SOFOG3D experiment, *EGUsphere*, 2024, 1–45, <https://doi.org/10.5194/egusphere-2024-1344>, 2024.
- 985 Egli, S., Maier, F., Bendix, J., and Thies, B.: Vertical distribution of microphysical properties in radiation fogs — A case study, *Atmospheric Research*, 151, 130–145, <https://doi.org/https://doi.org/10.1016/j.atmosres.2014.05.027>, sixth International Conference on Fog, Fog Collection and Dew, 2015.

- Fu, Q. and Liou, K. N.: On the Correlated k-Distribution Method for Radiative Transfer in Nonhomogeneous Atmospheres, *Journal of Atmospheric Sciences*, 49, 2139 – 2156, [https://doi.org/10.1175/1520-0469\(1992\)049<2139:OTCDMF>2.0.CO;2](https://doi.org/10.1175/1520-0469(1992)049<2139:OTCDMF>2.0.CO;2), 1992.
- Fu, Q. and Liou, K. N.: Parameterization of the Radiative Properties of Cirrus Clouds, *Journal of Atmospheric Sciences*, 50, 2008 – 2025, [https://doi.org/10.1175/1520-0469\(1993\)050<2008:POTRPO>2.0.CO;2](https://doi.org/10.1175/1520-0469(1993)050<2008:POTRPO>2.0.CO;2), 1993.
- George, J. J.: Fog, pp. 1179–1189, American Meteorological Society, Boston, MA, ISBN 978-1-940033-70-9, https://doi.org/10.1007/978-1-940033-70-9_95, 1951.
- 995 Gilardoni, S., Massoli, P., Giulianelli, L., Rinaldi, M., Paglione, M., Pollini, F., Lanconelli, C., Poluzzi, V., Carbone, S., Hillamo, R., Russell, L. M., Facchini, M. C., and Fuzzi, S.: Fog scavenging of organic and inorganic aerosol in the Po Valley, *Atmospheric Chemistry and Physics*, 14, 6967–6981, <https://doi.org/10.5194/acp-14-6967-2014>, 2014.
- Gultepe, I.: A Review on Weather Impact on Aviation Operations: Visibility, Wind, Precipitation, Icing, *Journal of Airline Operations and Aviation Management*, 2, <https://doi.org/10.5194/amt-16-2455-2023>, 2023.
- 1000 Gultepe, I., Pearson, G., Milbrandt, J. A., Hansen, B., Platnick, S., Taylor, P., Gordon, M., Oakley, J. P., and Cober, S. G.: The Fog Remote Sensing and Modeling Field Project, *Bulletin of the American Meteorological Society*, 90, 341 – 360, <https://doi.org/10.1175/2008BAMS2354.1>, 2009.
- Gultepe, I., Sharman, R., and et all.: A Review of High Impact Weather for Aviation Meteorology., *Pure Appl. Geophys.*, 176, 1869–1921, <https://doi.org/10.1007/s00024-019-02168-6>, 2019.
- 1005 Hagan, D. H. and Kroll, J. H.: Assessing the accuracy of low-cost optical particle sensors using a physics-based approach, *Atmospheric Measurement Techniques*, 13, 6343–6355, <https://doi.org/10.5194/amt-13-6343-2020>, 2020.
- Han, S.-Q., Hao, T.-Y., Zhang, M., Yao, Q., Liu, J.-L., Cai, Z.-Y., and Li, X.-J.: Observation Analysis on Microphysics Characteristics of Long-lasting Severe Fog and Haze Episode at Urban Canopy Top, *Aerosol and Air Quality Research*, 18, 2475–2486, <https://doi.org/10.4209/aaqr.2017.10.0416>, 2018.
- 1010 Kasper, D. M.: Slots, Property Rights and Secondary Markets: Efficiency and Slot Allocation at US Airports, Taylor and Francis, <https://doi.org/10.4324/9781315262963-27>, cited by: 5, 2016.
- Khain, A. P., Beheng, K. D., Heymsfield, A., Korolev, A., Krichak, S. O., Levin, Z., Pinsky, M., Phillips, V., Prabhakaran, T., Teller, A., van den Heever, S. C., and Yano, J.-I.: Representation of microphysical processes in cloud-resolving models: Spectral (bin) microphysics versus bulk parameterization, *Reviews of Geophysics*, 53, 247–322, <https://doi.org/https://doi.org/10.1002/2014RG000468>, 2015.
- 1015 Lakra, K. and Avishek, K.: A review on factors influencing fog formation, classification, forecasting, detection and impacts, *Rendiconti Lincei. Scienze Fisiche e Naturali*, 33, 319–353, 2022.
- Maronga, B. and Bosveld, F. C.: Key parameters for the life cycle of nocturnal radiation fog: a comprehensive large-eddy simulation study, *Quarterly Journal of the Royal Meteorological Society*, 143, 2463–2480, <https://doi.org/https://doi.org/10.1002/qj.3100>, 2017.
- Mason, J.: The Physics of Radiation Fog, *Journal of the Meteorological Society of Japan. Ser. II*, 60, 486–499, https://doi.org/10.2151/jmsj1965.60.1_486, 1982.
- 1020 Mazoyer, M., Lac, C., Thouron, O., Bergot, T., Masson, V., and Musson-Genon, L.: Large eddy simulation of radiation fog: impact of dynamics on the fog life cycle, *Atmospheric Chemistry and Physics*, 17, 13017–13035, <https://doi.org/10.5194/acp-17-13017-2017>, 2017.
- Mazoyer, M., Burnet, F., and Denjean, C.: Experimental study on the evolution of droplet size distribution during the fog life cycle, *Atmospheric Chemistry and Physics*, 22, 11305–11321, <https://doi.org/10.5194/acp-22-11305-2022>, 2022.
- 1025

- Mohammadi, M., Nowak, J. L., Bertens, G., Moláček, J., Kumala, W., and Malinowski, S. P.: Cloud microphysical measurements at a mountain observatory: comparison between shadowgraph imaging and phase Doppler interferometry, *Atmospheric Measurement Techniques*, 15, 965–985, <https://doi.org/10.5194/amt-15-965-2022>, 2022.
- Nowak, J. L., Mohammadi, M., and Malinowski, S. P.: Applicability of the VisiSize D30 shadowgraph system for cloud microphysical measurements, *Atmospheric Measurement Techniques*, 14, 2615–2633, <https://doi.org/10.5194/amt-14-2615-2021>, 2021.
- Nurowska, K., Mohammadi, M., Malinowski, S., and Markowicz, K.: Applicability of the low-cost OPC-N3 optical particle counter for microphysical measurements of fog, *Atmospheric Measurement Techniques*, 16, 2415–2430, <https://doi.org/10.5194/amt-16-2415-2023>, 2023.
- Okita, T.: Observations of the vertical structure of a stratus cloud and radiation fogs in relation to the mechanism of drizzle formation, *Tellus*, 14, 310–322, <https://doi.org/10.3402/tellusa.v14i3.9556>, 1962.
- Philip, A., Bergot, T., Bouteloup, Y., and Bouyssel, F.: The Impact of Vertical Resolution on Fog Forecasting in the Kilometric-Scale Model AROME: A Case Study and Statistics, *Weather and Forecasting*, 31, 1655 – 1671, <https://doi.org/10.1175/WAF-D-16-0074.1>, 2016.
- Pinnick, R. G., Hoihjelle, D. L., Fernandez, G., Stenmark, E. B., Lindberg, J. D., Hoidale, G. B., and Jennings, S. G.: Vertical Structure in Atmospheric Fog and Haze and Its Effects on Visible and Infrared Extinction, *Journal of Atmospheric Sciences*, 35, 2020 – 2032, [https://doi.org/10.1175/1520-0469\(1978\)035<2020:VSIAFA>2.0.CO;2](https://doi.org/10.1175/1520-0469(1978)035<2020:VSIAFA>2.0.CO;2), 1978.
- Pithani, P., Ghude, S., Naidu, c., Kulkarni, R., Steeneveld, G.-J., Sharma, A., Prabha, T., Chate, D., Gultepe, I., Jenamani, R., and Rajeevan, M.: WRF model Prediction of a dense fog event occurred during Winter Fog Experiment (WIFEX), *Pure and Applied Geophysics*, 176, 1827–1846, <https://doi.org/10.1007/s00024-018-2053-0>, 2019.
- Poku, C., Ross, A. N., Hill, A. A., Blyth, A. M., and Shipway, B.: Is a more physical representation of aerosol activation needed for simulations of fog?, *Atmospheric Chemistry and Physics*, 21, 7271–7292, <https://doi.org/10.5194/acp-21-7271-2021>, 2021.
- Price, J.: Radiation Fog. Part I: Observations of Stability and Drop Size Distributions, *Boundary-Layer Meteorology*, 139, 167–191, <https://doi.org/10.1007/s10546-010-9580-2>, 2011.
- Román-Cascón, C., Yagüe, C., Sastre, M., Maqueda, G., Salamanca, F., and Viana, S.: Observations and WRF simulations of fog events at the Spanish Northern Plateau, *Advances in Science and Research*, 8, 11–18, <https://doi.org/10.5194/asr-8-11-2012>, 2012.
- Stevens, S. E.: Trends in Instrument Flight Rules (IFR) Conditions at Major Airports in the United States, *Journal of Applied Meteorology and Climatology*, 58, 615 – 620, <https://doi.org/10.1175/JAMC-D-18-0301.1>, 2019.
- Thoma, C., Schneider, W., Masbou, M., and Bott, A.: Integration of Local Observations into the One Dimensional Fog Model PAFOG, *Pure and Applied Geophysics*, 169, 881–893, <https://doi.org/10.1007/s00024-011-0357-4>, 2011.
- Toledo, F., Haeffelin, M., Wærsted, E., and Dupont, J.-C.: A new conceptual model for adiabatic fog, *Atmospheric Chemistry and Physics*, 21, 13 099–13 117, <https://doi.org/10.5194/acp-21-13099-2021>, 2021.
- Wærsted, E. G., Haeffelin, M., Dupont, J.-C., Delanoë, J., and Dubuisson, P.: Radiation in fog: quantification of the impact on fog liquid water based on ground-based remote sensing, *Atmospheric Chemistry and Physics*, 17, 10 811–10 835, <https://doi.org/10.5194/acp-17-10811-2017>, 2017.
- Wendish, M., Mertes, S., Heintzenberg, J., Wiedensohler, A., Schell, D., Wobrock, W., Frank, G., Martinsson, B. G., Fuzzi, S., Orsi, G., Kos, G., and Berner, A.: Drop size distribution and LWC in Po valley fog, *Contributions to Atmospheric Physics*, 71, 87 – 100, <https://www.scopus.com/inward/record.uri?eid=2-s2.0-0031779779&partnerID=40&md5=9b5423094749ae926835f315751c4503>, cited by: 47, 1998.

Yau, M. and Rogers, R.: A Short Course in Cloud Physics, Elsevier Science, ISBN 9780080570945, <https://books.google.pl/books?id=CIKbCgAAQBAJ>, 1996.

1065 Ye, X., Wu, B., and Zhang, H.: The turbulent structure and transport in fog layers observed over the Tianjin area, *Atmospheric Research*, 153, 217–234, <https://doi.org/https://doi.org/10.1016/j.atmosres.2014.08.003>, 2015.

Zhou, B., Du, J., Gultepe, I., and Dimego, G.: Forecast of Low Visibility and Fog from NCEP: Current Status and Efforts, *Pure and Applied Geophysics*, 169, 895–909, <https://doi.org/10.1007/s00024-011-0327-x>, 2012.

Appendix A: Temperature set up in the model

1070 The data about T and RH ~~where were~~ taken from HYT and GY-63 and interpolated to ~~levels of the levels of the~~ model. As the measurements ~~where were~~ mostly reaching 115 m, above the ~~T~~temperature and humidity profile ~~were was~~ set according to the measurement from atmospheric sounding from Tarnów (WMO station 12575) done by IMGW (Polish Institute of Meteorology and Water Management). Tarnów is 60 km in ~~a~~ straight line from Strzyżów city. For ~~a~~ better description of the merging of data sounding from Tarnów will be called soundingT.

1075 To have a smooth transition between balloon sounding and the soundingT, the data from the balloon and soundingT were stitched together. For this purpose ~~first~~, ~~first~~, the points were extrapolated so that at the stitching point, the values from both soundings were available. The procedure was performed for the last three points (highest points) from the balloon profile and ~~the~~ first two points of soundingT above ~~the~~ balloon profile. Then, ~~for~~ these five points, the average value weighted by the distance of the points was taken. As the soundingT ~~does~~ not always reach 10km, above soundingT the standard atmosphere
1080 profile for mid-latitude summer was used.

As ~~the~~ profile of RH was stitched and interpolated, the precipitable water (PW) was changed. To fix this issue, the whole profile of RH has been rescaled in such a way that PW is the same as the PW obtained from soundingT before interpolating.

Appendix B: Additional Tables and Figures

sounding nr	Day	Time	Radioonde AE-51	GY63	HYT	OPC-N3	SPS30	sounding nr	Day	Time	Radioonde AE-51	GY63	HYT	OPC-N3	SPS30	sounding nr	Day	Time	Radioonde AE-51	GY63	HYT	OPC-N3	SPS30
1	08	20:29 - 20:42	☐					28	09	17:59 - 18:10	● ●					54	11	02:11 - 02:17		▶	▶	▶	▶
2	08	21:00 - 21:35	☐					29	10	00:41 - 00:51		☐	☐	☐	☐	55	11	02:19 - 02:26		☐	☐	☐	☐
3	08	22:24 - 22:34		☐	☐	☐	☐	30	10	00:53 - 01:05	●					56	11	02:29 - 02:37		☐	☐	☐	☐
4	09	00:22 - 00:28		▶	▶	▶	▶	31	10	01:18 - 01:28		☐	☐	☐	☐	57	11	02:43 - 03:02	●				
5	09	00:30 - 00:40		▶	▶	▶	▶	32	10	01:37 - 01:46		☐	☐	☐	☐	58	11	03:10 - 03:20		▶	▶	▶	▶
6	09	00:48 - 01:01	●					33	10	01:55 - 02:04	●					59	11	03:23 - 03:33		▶	▶	▶	▶
7	09	01:20 - 01:27		▶	▶	▶	▶	34	10	02:24 - 02:34		▶	▶	▶	▶	60	11	03:36 - 03:46		▶	▶	▶	▶
8	09	01:32 - 01:41		▶	▶	▶	▶	35	10	02:40 - 02:48		▶	▶	▶	▶	61	11	03:49 - 03:59	●				
9	09	02:34 - 02:42		▶	▶	▶	▶	36	10	02:54 - 03:06		▶	▶	▶	▶	62	11	04:04 - 04:16		▶	▶	▶	▶
10	09	02:45 - 02:55		▶	▶	▶	▶	37	10	03:09 - 03:23	●					63	11	04:19 - 04:36		▶	▶	▶	▶
11	09	03:03 - 03:27	●					38	10	03:33 - 03:44		▶	▶	▶	▶	64	11	04:40 - 04:56		▶	▶	▶	▶
12	09	03:34 - 04:03		▶	▶	▶	▶	39	10	03:49 - 04:00		▶	▶	▶	▶	65	11	04:59 - 05:15	●				
13	09	04:09 - 04:22		▶	▶	▶	▶	40	10	04:06 - 04:17		▶	▶	▶	▶	66	11	05:19 - 05:30		▶	▶	▶	▶
14	09	05:10 - 05:21		▶	▶	▶	▶	41	10	04:20 - 04:40	●					67	11	05:32 - 05:45		▶	▶	▶	▶
15	09	05:23 - 05:34		▶	▶	▶	▶	42	10	04:50 - 05:00		▶	▶	▶	▶	68	11	05:47 - 05:59		▶	▶	▶	▶
16	09	05:37 - 05:45		▶	▶	▶	▶	43	10	05:06 - 05:21		▶	▶	▶	▶	69	11	06:02 - 06:11	● ●				
17	09	05:47 - 05:54	▲	▲	▲	▲	▲	44	10	05:25 - 05:37		▶	▶	▶	▶	70	11	06:18 - 06:33	● ●				
18	09	05:56 - 06:06	▲	▲	▲	▲	▲	45	10	05:40 - 05:56	●					71	11	06:39 - 06:53		▶	▶	▶	▶
19	09	06:09 - 06:17	▲	▲	▲	▲	▲	46	10	06:03 - 06:13		☐	☐	☐	☐	72	11	06:56 - 07:14	● ●				
20	09	06:19 - 06:28	▲	▲	▲	▲	▲	47	10	06:23 - 06:31		▶	▶	▶	▶	73	11	07:15 - 07:29	● ●				
21	09	06:33 - 06:42	▲	▲	▲	▲	▲	48	10	06:31 - 06:40		▶	▶	▶	▶	74	11	07:36 - 07:51	● ●				
22	09	06:45 - 06:53	▲	▲	▲	▲	▲	49	10	06:42 - 06:50	● ●												
23	09	06:56 - 07:03	▲	▲	▲	▲	▲	50	10	06:52 - 07:00		☐	☐	☐	☐								
24	09	07:07 - 07:13	▲	▲	▲	▲	▲	51	10	07:01 - 07:19	● ●												
25	09	07:18 - 07:41	● ●					52	10	07:11 - 07:17		☐	☐	☐	☐								
26	09	07:42 - 07:56	● ●					53	10	07:22 - 07:32	● ●												
27	09	07:57 - 08:08	● ●																				

Table A1. Apparatus used during each of the soundings of case study [8-9](#) - 11 [September-Sep](#), 2023. Markers [representsrepresent](#): ▶ - setup with OPC-N3, ● - setup with radiosonde, ▲- setup with OPC-N3 and radiosonde, ☐ - problems with collected data (sounding with partially recorded data were not taken into further analysis).

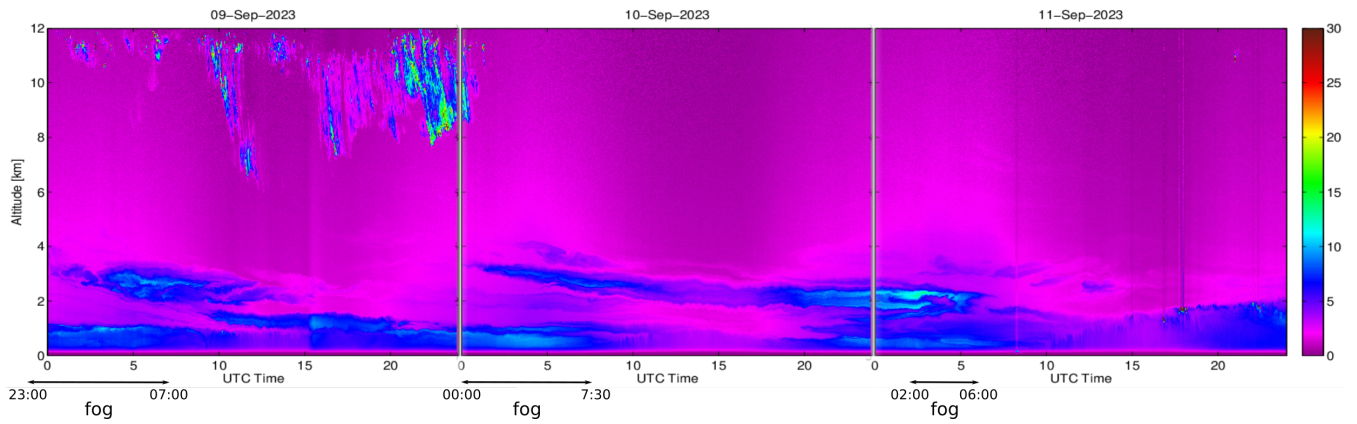
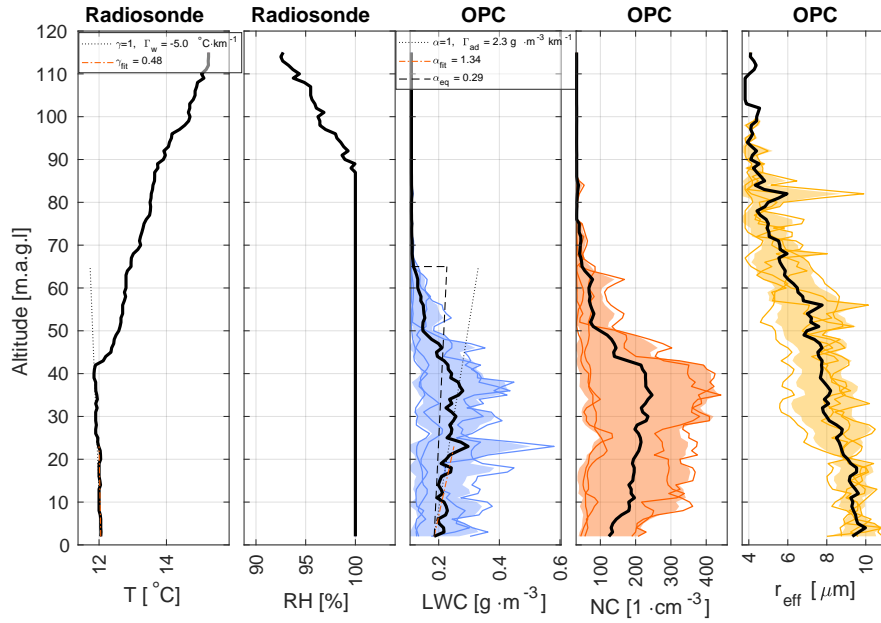


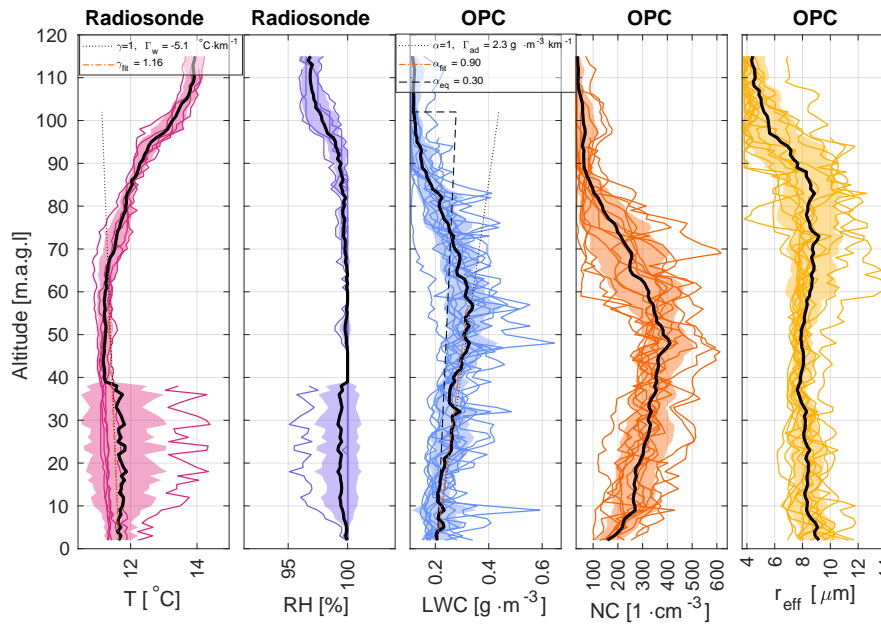
Figure A1. Temporal variability of 510M lidar range corrected signal (at 532 nm) from [the](#) level of the upper station up to 12 km between 9 and 11 ~~September~~ [Sep.](#) 2023.



Figure A2. Visualization of radiation fog top. Photos were taken with the camera at the SolarAOT^{upper} station at 4 UTC each day.

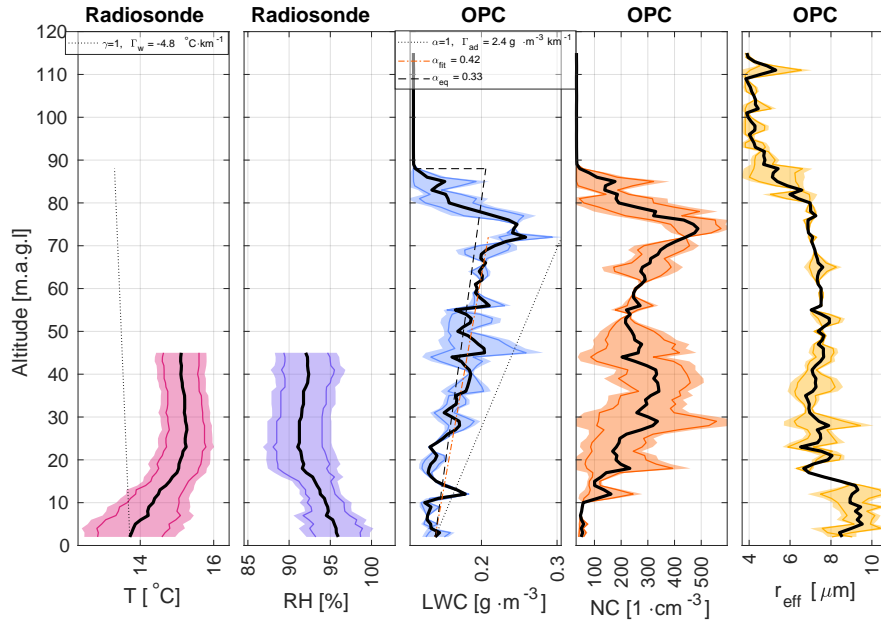


(a) Development stage of fog.



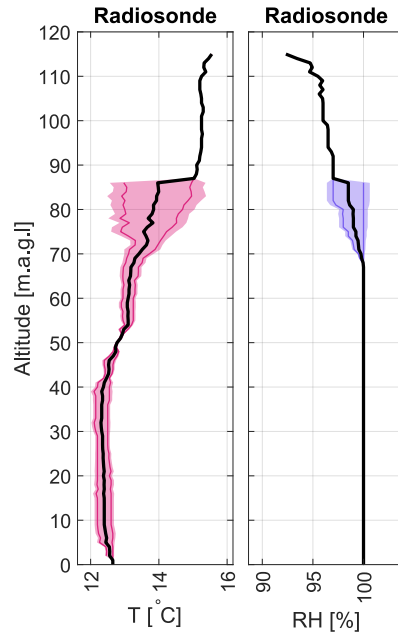
(b) Mature state of fog.

Figure A3. Figures presents present specific quantities measured by the balloon for each stage of fog observed during night 08-09 Sep. 2023.

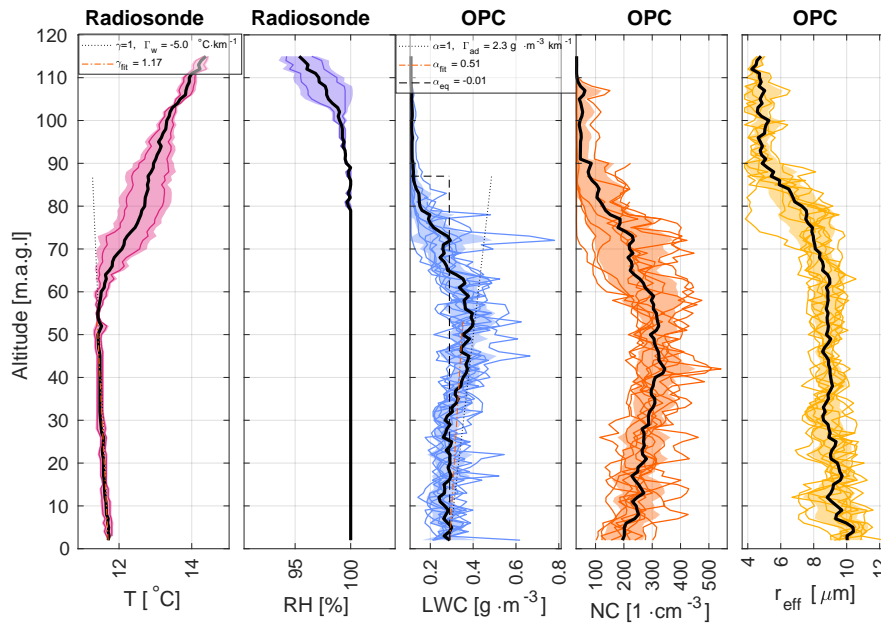


(c) Disappearing stage of fog

Figure A3. Figures presents present specific quantities measured by the balloon for each stage of fog observed during night 08-09 Sep. 2023. From left: T from Vaisala radiosonde RS41, RH from Vaisala radiosonde RS41, N_c , r_{eff} within the fog. Each colored line represents one balloon profile. ~~Black~~The black thick line represents the mean of all the soundings, the colored area represents the range in-between +/- standard deviation from the mean. At the T plot dotted line presents the lapse rate, dashed red line presents the linear fit to T from 32 m to the height of maximum mean LWC. At the LWC plot dotted line presents the LWC adiabatic lapse rate, the dashed red line presents the linear fit to LWC from 32 m to the height of maximum mean LWC.

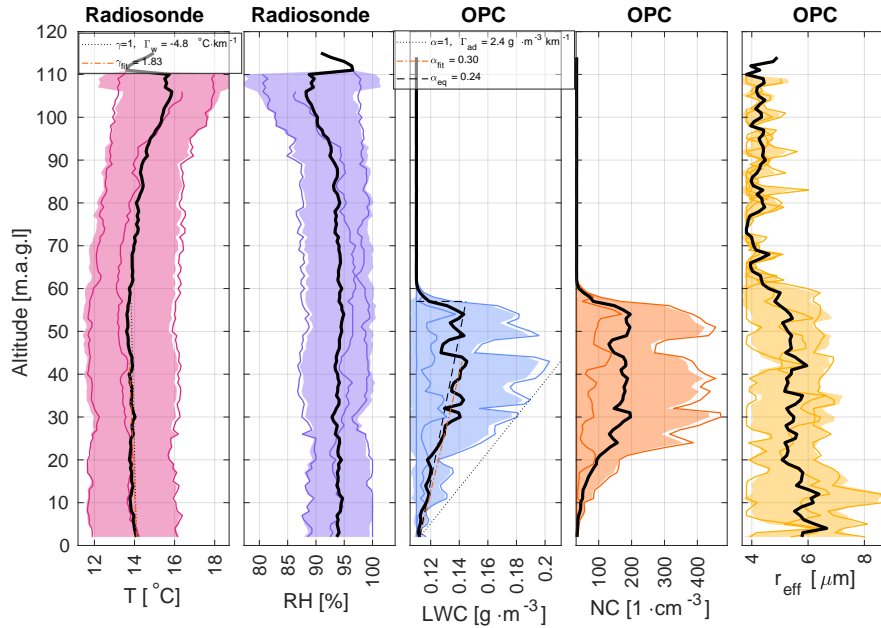


(a) Development stage of fog.



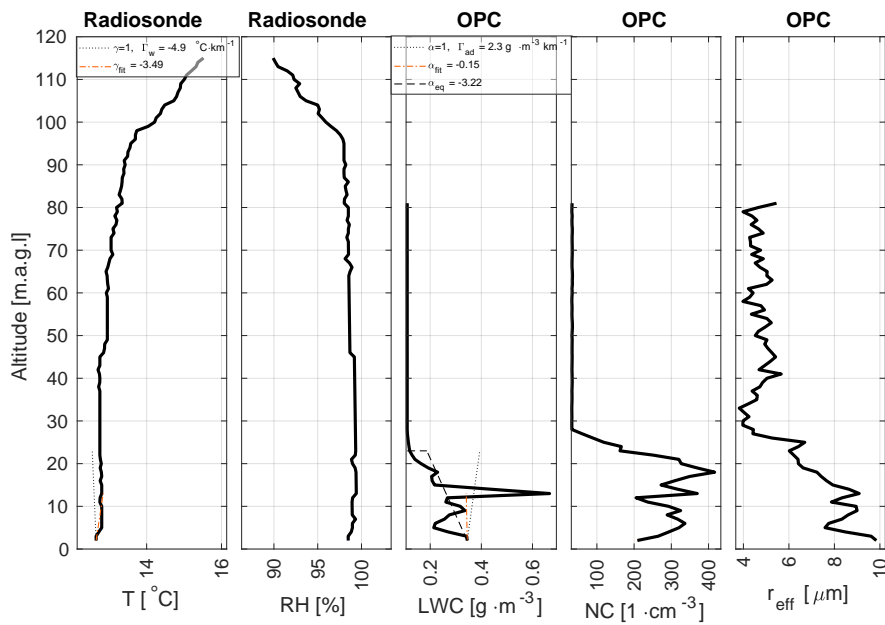
(b) Mature state of fog.

Figure A4. Figures presents present specific quantities measured by the balloon for each stage of fog observed during night 10-11 Sep. 2023.



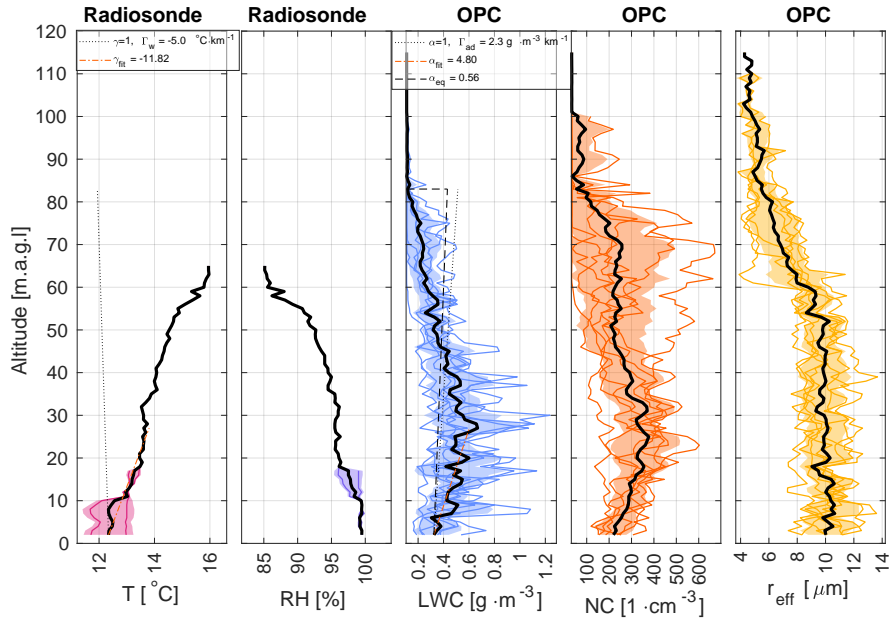
(c) Disappearing stage of fog

Figure A4. Figures presents present specific quantities measured by the balloon for each stage of fog observed during night 09-10 Sep. 2023. From left: T from Vaisala radiosonde RS41, RH from Vaisala radiosonde RS41, N_c , r_{eff} within the fog. Each colored line represents one balloon profile. Black-The black thick line represents the mean of all the soundings, the colored area represents the range in-between +/- standard deviation from the mean. At the T plot dotted line presents the lapse rate, dashed red line presents the linear fit to T from 32 m to the height of maximum mean LWC. At the LWC plot dotted line presents the LWC adiabatic lapse rate, the dashed red line presents the linear fit to LWC from 32 m to the height of maximum mean LWC.

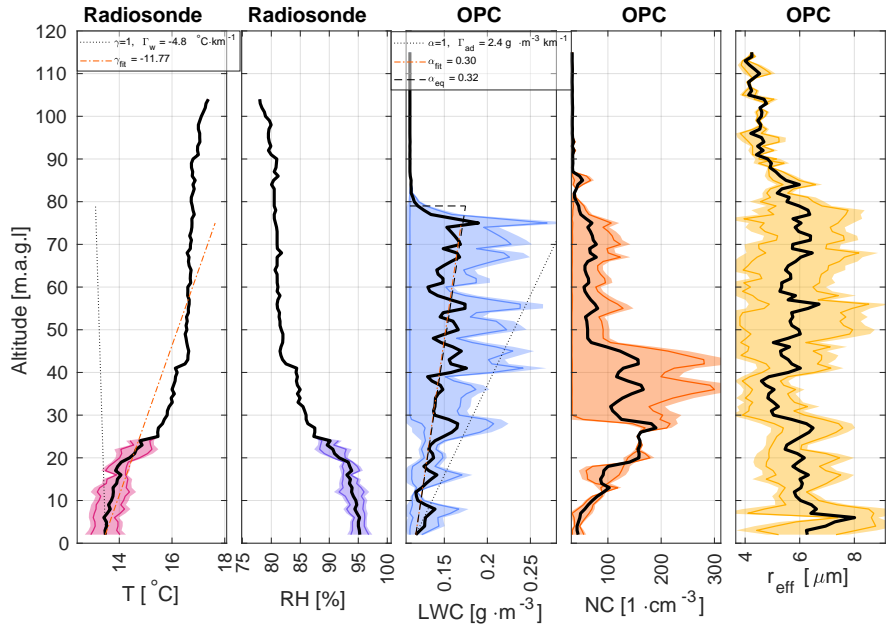


(a) Development stage of fog.

Figure A5. Figures presents present specific quantities measured by the balloon for each stage of fog observed during night 10-11 Sep. 2023.



(b) Mature state of fog.



(c) Disappearing stage of fog

Figure A5. Figures presents present specific quantities measured by the balloon for each stage of fog observed during night 10-11 Sep. 2023. From left: T from Vaisala radiosonde RS41, RH from Vaisala radiosonde RS41, N_c , r_{eff} within the fog. Each colored line represents one balloon profile. **Black-The black** thick line represents the mean of all the soundings, **the** colored area represents **the** range in-between \pm standard deviation from the mean. At the T plot dotted line presents the lapse rate, dashed red line presents the linear fit to T from 32 m to **the** height of maximum mean LWC. At the LWC plot dotted line presents the LWC adiabatic lapse rate, **the** dashed red line presents the linear fit to LWC from 32 m to **the** height of maximum mean LWC.

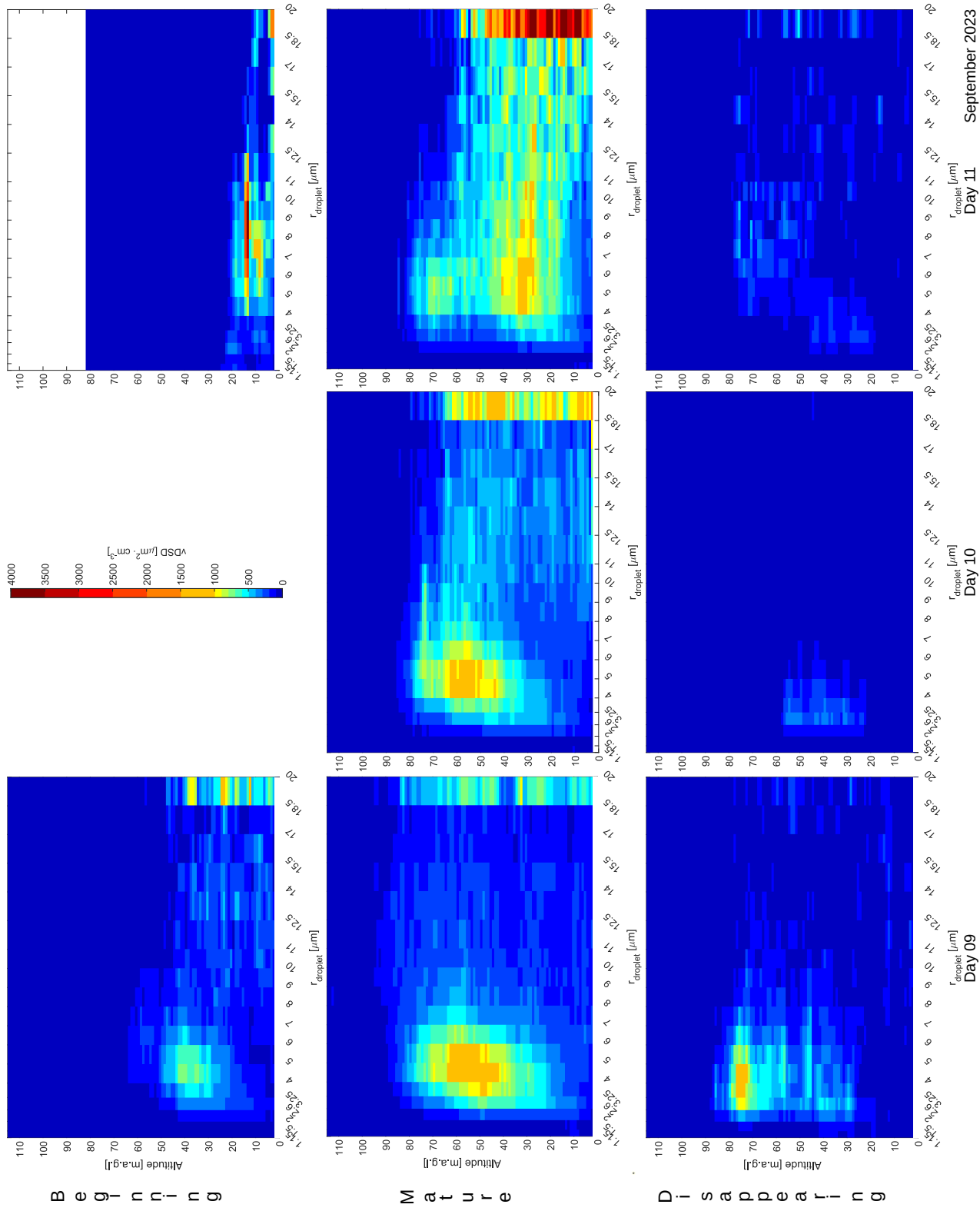


Figure A6. Profiles with height of vDSD for [8-11 September 9-11 Sep. 2023](#) fog occurrence. In columns different days, in rows from top: beginning, mature, and disappearing stage of fog.